

Article

Effect of Basic Promoters on Porous Supported Alumina Catalysts for Acetins Production

Rita de Cássia F. Bezerra ¹, Gabriela Mota ¹, Ruth Maria B. Vidal ¹, Jose Vitor do Carmo ¹, Gilberto D. Saraiva ², Adriana Campos ³, Alcineia C. Oliveira ^{1,*}, Rossano Lang ⁴, Larissa Otubo ⁵, José Jiménez Jiménez ⁶ and Enrique Rodríguez-Castellón ^{6,*}

¹ Departamento de Química Analítica e Físico-Química, Universidade Federal do Ceará, Campus do Pici, Bloco 940, Fortaleza 60455-760, Brazil

² Faculdade de Educação Ciências e Letras do Sertão Central, Universidade Estadual do Ceará, Quixadá 63902-098, Brazil

³ CETENE, Cidade Universitária, Recife 50740-545, Brazil

⁴ Instituto de Ciência e Tecnologia, Universidade Federal de São Paulo—UNIFESP, São José dos Campos 12231-280, Brazil

⁵ Centro de Ciência e Tecnologia de Materiais—CCTM, Instituto de Pesquisas Energéticas e Nucleares—IPEN, São Paulo 05508-000, Brazil

⁶ Departamento de Química Inorgánica, Facultad de Ciencias, Universidad de Málaga, 29071 Málaga, Spain

* Correspondence: alcineia@ufc.br (A.C.O.); castellon@uma.es (E.R.-C.)

Abstract: A facile strategy for the design of porous supports was obtained by modifying the sol-gel method followed by the wet impregnation technique. In this respect, herein, the acidity of the γ -Al₂O₃ phase was modulated by adding basic MgO, La₂O₃ or ZnO promoters to form binary supported catalysts. The Ni and Co dispersion on the supports associated with their tunable acidity and morphologies resulted in highly porous supported alumina-based catalysts. The physicochemical properties of the solids were comprehensively investigated by XRD, textural properties, Raman and FTIR spectroscopy, SEM-EDS, TEM, EPR and XPS analyses. The catalytic performances in the esterification of glycerol in the presence of acetic acid (EG) for the acetins production were evaluated. The highly dispersed NiO and Co₃O₄ active species on binary porous supports produced synergistic effects appearing to be the reason for the activity of the solids in the EG reaction. Under the optimized reaction conditions, NiCo/MgO-Al₂O₃ was found to be a robust solid with superior catalytic performance and improved stability in four reaction cycles with 65.0% of glycerol conversion with an exclusive selectivity of 53% for triacetin. The presence of Co²⁺/Co³⁺ and Ni²⁺ strongly interacting with the spinel γ -Al₂O₃ and MgAl₂O₄ phases, the latter having a large number of lattice oxygen species, was considered another active component besides those of Ni and Co in the esterification of glycerol.

Keywords: porous alumina; support; esterification; glycerol; basic promoters



Citation: Bezerra, R.d.C.F.; Mota, G.; Vidal, R.M.B.; Carmo, J.V.d.; Saraiva, G.D.; Campos, A.; Oliveira, A.C.; Lang, R.; Otubo, L.; Jiménez Jiménez, J.; et al. Effect of Basic Promoters on Porous Supported Alumina Catalysts for Acetins Production. *Catalysts* **2022**, *12*, 1616. <https://doi.org/10.3390/catal12121616>

Academic Editor: Narendra Kumar

Received: 29 October 2022

Accepted: 5 December 2022

Published: 9 December 2022

Publisher's Note: MDPI stays neutral with regard to jurisdictional claims in published maps and institutional affiliations.



Copyright: © 2022 by the authors. Licensee MDPI, Basel, Switzerland. This article is an open access article distributed under the terms and conditions of the Creative Commons Attribution (CC BY) license (<https://creativecommons.org/licenses/by/4.0/>).

1. Introduction

In recent decades, glycerol valorization has received prominent research interest because of escalating biodiesel production [1–3]. The large amounts of crude glycerol as the main by-product of the biodiesel industries have impelled the scientific community to look for alternatives to convert the trialcohol into value-added chemicals [1–6].

To date, many catalytic routes, including dehydration, esterification, reforming and acetalization, among others, have been developed to utilize processes capable of consuming raw glycerol for industrial applications [4–8]. Particularly, the esterification reaction of glycerol in the presence of acetic acid (EG) becomes increasingly important for the direct use of glycerol to obtain more valuable products (Figure 1).

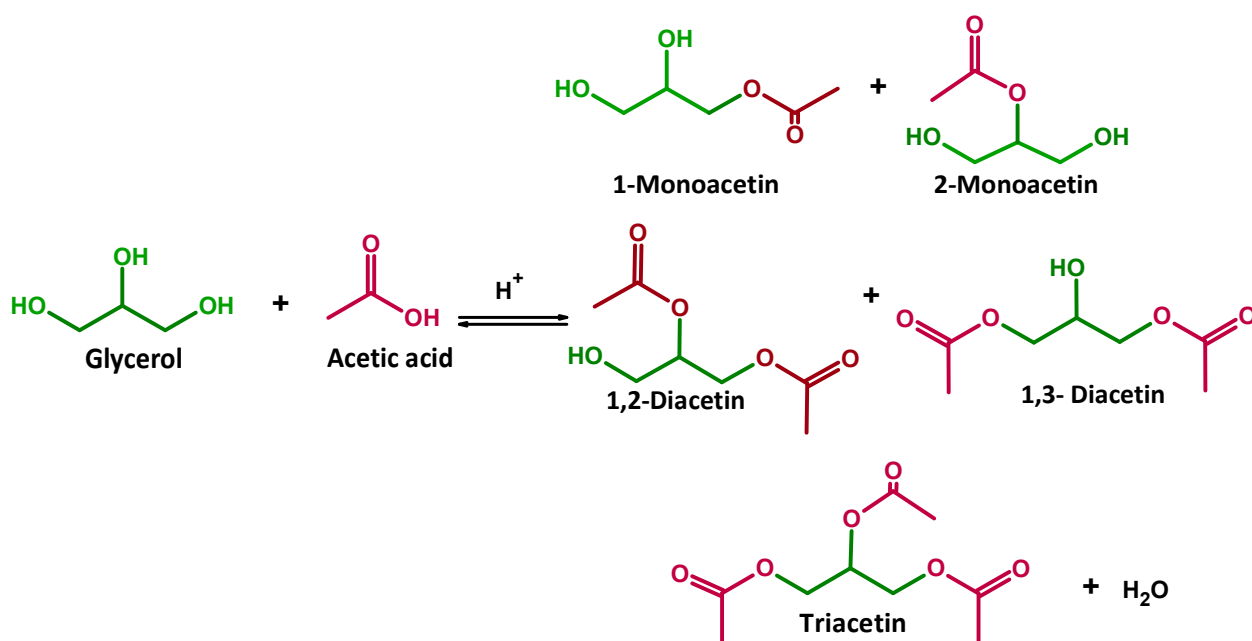


Figure 1. Schematic illustration of the EG reaction in the presence of acetic acid.

Thus, the transformation of glycerol into glycerol esters (acetins) through the EG reaction is of commercial importance, since the obtained acetins are applied as emulsifiers, cosmetics, food additives, stabilizers, biofuels additives and pharmaceuticals [9–11]. This has boosted progress in the design of a variety of advanced catalytic materials towards the EG reaction, such as zeolites, resins, graphene oxide, metal oxides, amorphous and mesoporous sulfated silicas, hydroxyapatites and a diversity of supported oxides [1–7,11–13]. Among all types of catalysts, acid-based solids have been intensively investigated to produce acetins because of their good prospect for improving catalytic activities and yields during EG reaction [2,4,11–16].

In this sense, the exceptional properties of alumina-based catalysts, such as porosity, large specific surface area, chemical stability and their addressable Lewis and Brønsted acid sites for glycerol conversion, have made them of particular interest in the EG reaction [3,13,17–20]. However, the main disadvantages of these types of solid acid catalysts for glycerol esterification are their low water tolerance, leaching of active sites and low selectivities to the acetins, which significantly restrict their performance in the reaction [5,17–20]. Overall, strategies for acidity modulation of the catalysts that permit the control of acid strength, types of acid sites and surface acidity to minimize the problem on water deactivation and subsequently improving the selectivity of diacetin and triacetin are vastly documented [6,11,15,20].

It is particularly interesting to note that the current efforts for enhancing the performance of the solids in the EG reaction are moving towards the use of catalysts possessing simultaneous acid-based and redox active sites to the title reaction [5]. Such a bifunctional catalyst represents an emerging strategy to have a robust catalyst for glycerol esterification that at least limits the rapid deactivation by water of the active sites. Among the many attempts to overcome these limitations, synthetic methodologies to improve the accessibility of acid sites and increase the reactivity of surfaces are reasonably mature [2,10,21]. Nonetheless, little attention has been focused on the influence of the acidity modulation of the alumina-based catalysts and the consequent modification of their properties to achieve good catalytic performances [5,21,22].

In the present study, the effect of the basic promoters addition to supported alumina catalyst was investigated in the EG reaction for acetins production. This type of bifunctional catalyst involves the combination of Ni and Co species representing the active sites dispersed on the alumina support, besides tuning their acidic properties provided by the incorporation of MgO, ZnO and La₂O₃. Because the decline in acidity of the alumina

is known to be strongly influenced by the type of basic promoter [22–28], the suitable modification of the solid by MgO, ZnO or La₂O₃ seems to be well suited for solid textural properties and stability preservation, which would further alleviate the water deactivation in EG reaction and thus to improve the overall selectivity to the acetins.

Another important aspect of the synthesis of the catalysts under study is the efficiency of the sol-gel method to prevent particle aggregation and generate the porosity and accessibility of the acid sites to the reactant molecules [22–24]. It can be expected that a significant enhancement in catalytic properties can be achieved by combining the advantages of well dispersed Ni and Co sites on porous modified alumina possessing weak to medium acid site strengths. The physicochemical properties of the solids were intensively investigated by XRD, N₂-physisorption, Raman and FTIR spectroscopy, SEM-EDS, TEM, EPR and XPS measurements.

2. Results and Discussion

2.1. Structural Characterizations

XRD patterns are collected to illustrate the structural features of the aluminas, after the incorporation of the basic promoters. A typical XRD pattern of the semi-crystalline γ -Al₂O₃ phase is clearly recognized by the low intensity and broad peaks (Figure 2a). Accordingly, small reflections at 2 θ values of 19.9, 31.2, 37.0, 39.8, 45.4, 60.7 and 67.1° are assigned to the (111), (220), (311), (222), (400), (511) and (440) crystallographic planes of the face centered-cubic Fd-3m planes for γ -Al₂O₃ phase (JCPDS 10-425). Notably, the most intense peaks of cubic γ -Al₂O₃ are depicted at 2 θ values of ca. 45.4 and 67.1° having quite similar intensities, except to MA sample. This allows us to deduce that the prevalence of γ -Al₂O₃ phase in all samples is related to the successful introduction of foreign oxides, such as ZnO, MgO and La₂O₃ into alumina lattice structure to form intermingled mixed-metal oxides.

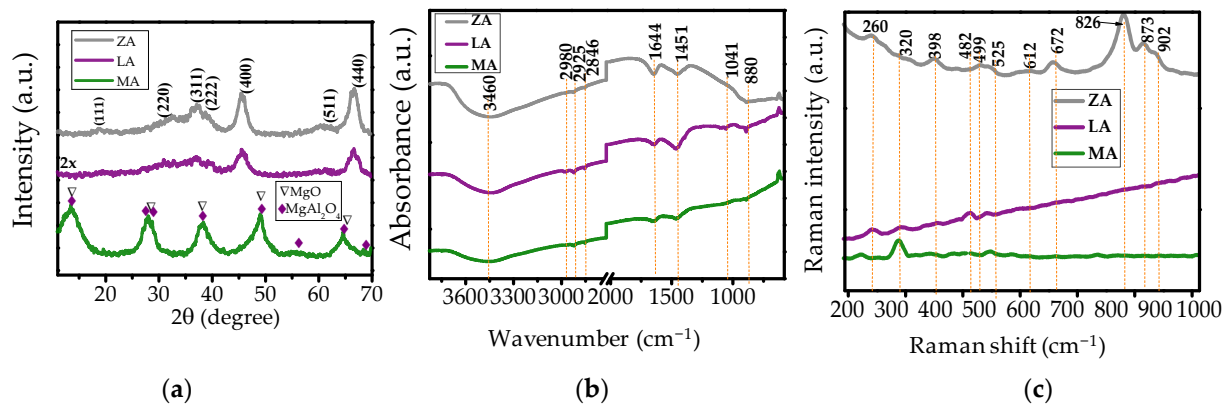


Figure 2. Physicochemical characterizations of the supports: (a) XRD, (b) FTIR and (c) Raman measurements. The letters LA, ZA, MA represent the La₂O₃-Al₂O₃, ZnO-Al₂O₃ and MgO-Al₂O₃ supports, respectively. The XRD pattern of LA sample is amplified 2× in Figure 2a.

To prove this hypothesis, XRD patterns of the unsupported samples (Figure 2a) reveal no detectable differences for a γ -Al₂O₃ sample, as found elsewhere [10,13,21]. It is supposed that the incorporation of the aforesaid basic oxides occurs because of the use of single-source alkoxy precursors, which form pre-existing Me-O-Al bonds via sol-gel chemistry process, where Al³⁺ (50 pm) cations are replaced by larger La³⁺ (105 pm), Zn²⁺ (75 pm) or Mg²⁺ (78 pm) during the synthesis [21,23,24]. Some others but very similar preparations of alumina are used with basic promoters resulting in weaker XRD peaks, which suggests the inclusion of the basic promoters into the cubic structure [25–28]. Obviously, weak diffraction peaks for LA indicate poor crystallinity due to either small particles or amorphous structure related to La₂O₃ oxides, but reflections of the γ -Al₂O₃ phase prevail in the solid. On the contrary, the diffraction peaks of ZA have a higher intensity than those of LA owing to the existence of the inherently larger particles in the former. For MA, a particular composition

of both cubic MgO and spinel MgAl_2O_4 phases is seen, probably due to the high calcination temperatures above $800\text{ }^\circ\text{C}$ favoring the spinel phase formation besides that of $\gamma\text{-Al}_2\text{O}_3$. The findings also state that the diffraction peaks are shifted to small 2θ values because of the lattice parameters of $\gamma\text{-Al}_2\text{O}_3$ increase caused by cell expansion, which evidences that some divalent Mg ions with larger ionic radius enter into the spinel skeleton by isomorphic replacement of Al^{3+} ions [29].

FTIR measurements are used to further characterize the structural features of the solids. Figure 2b shows the FTIR spectra of unsupported samples. A broad absorption band centered at 3460 cm^{-1} is visible with low intensity for all samples, which corresponds to the hydrogen-bonded O–H stretching $\nu(\text{O-H})$ of physisorbed water. Another possible assignment of this band could be the structural hydroxyl groups present in the oxides, which is consistent with previous reports [13,30]. Moreover, weak absorption bands emerged at approximately 1644 cm^{-1} are assigned to the bending vibration $\delta(\text{O-H})$ of hydroxyl groups (Figure 2b). Moreover, the stretchings of the alkyl groups $\nu(\text{C-H})$ are located at 2980 , 2925 , and 2846 cm^{-1} . Furthermore, the band observed at 1041 cm^{-1} for the unsupported solids could be due to C–O stretching of the carbonyl groups, which are not completely removed upon calcination.

Raman spectroscopy is helpful to complement the structural investigation of solids. Raman spectra of the unsupported solids are characterized by the presence of four weak bands located in the low-frequency region at approximately 260 , 320 , 482 and 672 cm^{-1} (Figure 2c). According to the findings, the corundum-type structure, e.g., $\gamma\text{-Al}_2\text{O}_3$ phase has a D_{3d}^6 symmetry with seven Raman active phonon modes and the signals assigned as those of $2A_1g+5E_g$ modes are observed at 378 , 418 , 432 , 451 , 578 , 645 and 751 cm^{-1} [30,31]. This is in agreement with the bands found in the FTIR spectra. The Raman band at 260 cm^{-1} is slightly shifted to lower frequencies within $2\text{--}20\text{ cm}^{-1}$ range possibly due to Mg–O bonds from free MgO and MgAl_2O_4 species on solid surface of MA support, as evidenced by XRD.

Additionally, the corundum structure may also depict a strong fluorescence background without visible Raman bands for the $\gamma\text{-Al}_2\text{O}_3$ phase, depending on the calcination temperature and laser excitation and power of the source used [30,31]. Interestingly, long exposure times, such as 50 scans applied to the samples under study allow the observed weak Raman bands for the unsupported samples. This clearly suggests that the aforesaid signals are consistent with the Al–O–Al vibrational modes in AlO_6 octahedra [30,31]. Additional signals appearing at approximately 398 , 499 , 525 , 612 , 826 , 873 and 902 cm^{-1} are clearly detectable for ZA support (Figure 2c). Such type of signals could be a hexagonal wurtzite structure of ZnO belonging to the $P6_3mc$ (C_{6v}) space group [32], mostly coming from some ZnO on the solid surface. Although ZnO contributions are not observable by XRD results, Raman spectroscopy is very sensitive to detect surface species. Instead, XRD measurements are devoted to observing the bulk species. In addition, other contributions of the MgO or MgAl_2O_4 and La_2O_3 promoters to the Raman spectra are not observable, which indicates the inclusion of these oxides in the alumina host, in line with XRD measurements (Figure 2a). These results are later confirmed by TEM measurements.

It seems that the XRD peak positions and intensities remain unchanged, after the dispersion of relatively low Ni and Co amounts on the surface of binary supports (Figure 3a). The NiCo/MA is an exception owing to the reflections of cubic MgO (JCPDS 89-7746) or spinel cubic MgAl_2O_4 (JCPDS 9-1627) appearing in the diffractograms. Furthermore, NiO nanoparticles are initially formed in the first impregnation step, whereas the subsequent Co_3O_4 nanoparticles co-impregnation process results in a high dispersion the aforesaid oxide species (Figure 3a). Hence, the peaks of the supported solids have similar intensities to those of the unsupported catalysts (Figure 2a). Additionally, it is not possible to rule out that the relatively low Ni and Co amounts on the support has little influence on the XRD diffractograms, due to the detection limit of the technique. Accordingly, the existence of the NiAl_2O_4 and CoAl_2O_4 spinel-like phases in the form of nanoparticles cannot be neglected due to the high dispersed and isolated Ni^{2+} and Co^{2+} interacting with alumina [30–33].

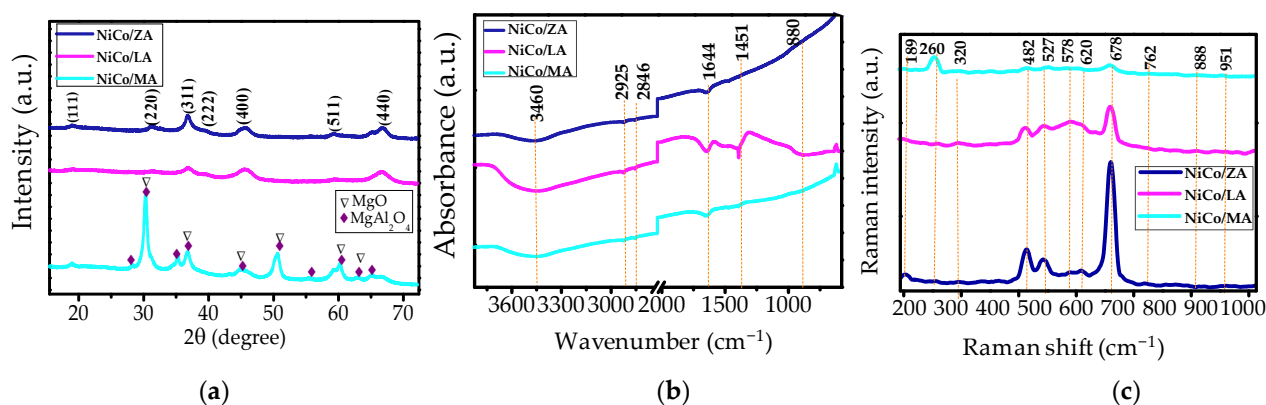


Figure 3. Physicochemical characterizations of the supported samples: (a) XRD, (b) FTIR and (c) Raman measurements. The letters NiCo/LA, NiCo/ZA and NiCo/MA represent the NiCo/La₂O₃-Al₂O₃, NiCo/ZnO-Al₂O₃ and NiCo/MgO-Al₂O₃ supported catalysts, respectively.

Interestingly, a noticeable increase in the FTIR band intensity at 1644 cm⁻¹ implies that a large fraction of the hydroxyl groups is intensified from the samples, after impregnating the metal oxides on the supports (Figure 3b). It could indicate the presence of more surface OH groups, after the support of the active components on alumina. As found elsewhere, dehydroxylation of supports after consecutive impregnation and calcination steps is a common phenomenon found in the preparation of the supported oxide catalysts [30]. This apparent discrepancy is explained based on the fact the above FTIR results confirm a significant enhancement of hydrophobicity through the generation of surface acid Brønsted sites, owing to the successful synthesis of porous materials.

The medium intensity band at 1451 cm⁻¹ for the supported samples is assigned the bending δ(C-H) vibrations of the organic compounds, such as residual trisec-butoxy aluminum [13]. This means that the precursors are not completely removed when calcinating the supports (Figure 3b). Further EDS and XPS results assign the presence of these residual carbon species on the solid surface. On the contrary, the disappearance or intensity attenuation of the residual carbon absorption bands in the spectra may be ascribable to the double calcination step of the metal oxides, after the impregnation process for supported samples (Figure 3b).

FTIR spectra of the supported solids (Figure 3b) do not exhibit representative bands at approximately 1041 cm⁻¹, which suggests the remaining trisec butoxyl groups removal from the solids after various calcination steps. At low frequency regions, the bands below 880 cm⁻¹ are assigned to Me-O lattice vibrations from stretching Me-OH, Me-O-Me or even O-Me-O bonds [22,30,33].

Raman spectra of the supported samples display distinct features compared with those of the unsupported solids (Figure 3c). Low frequencies bands positioned at approximately 260, 320, 482 and 678 cm⁻¹ attributable to the γ-Al₂O₃ phase remain unperturbed, but intensity change of other bands occurred simultaneously with the appearance of a broad band with little signals located at 480, 527, 578 and 620 cm⁻¹. Literature reports reveal that crystalline NiO has a defect rocksalt cubic structure (space group *Fm3m*) with Ni²⁺ cations in octahedral sites with Raman bands 460–600 cm⁻¹ [34–36]. Therefore, the observed broad band between 480–620 cm⁻¹ is attributed to the NiO nanoparticles dispersed on the supports. These observations are also consistent with the FTIR measurements, which reveal the presence of Me-O vibrations in the high frequencies region. In addition, Raman spectroscopy is capable of detecting surface nickel oxide nanoparticles in comparison with the XRD technique, which is sensitive to bulk species [34]. Bands found at approximately 189, 482, 527, 620 and 678 cm⁻¹ may also be attributed to the Raman active modes of Co₃O₄. Accordingly, cubic Co₃O₄ crystallizes in the normal spinel structure Co²⁺(Co³⁺)₂O₄²⁻ belonging to the *Fd3m* space group (*O_h⁷*) [36]. Hence, the cubic spinel lattice has Co²⁺ and Co³⁺ ions placed at tetrahedral and octahedral sites, respectively. The active *A_{1g}*, *E_g* and

3F2g Raman modes for the spinel structure are active in opposite to the 4F1u mode, which is infrared active. Accordingly, the Raman mode positioned at 189 cm^{-1} is ascribable to F2g phonon modes, meanwhile those at 482 and 678 cm^{-1} correspond to the Eg and A1g phonon modes, respectively [36].

In particular, the NiCo/MA sample has Raman bands at approximately 250 (F2g), 307 (F2g), 410 (F2g), 492 (F2g), 670 (F2g) and 762 (A1g) cm^{-1} that can be attributed to lattice vibrations of MgAl_2O_4 along with bands at approximately 410 , 670 and 762 cm^{-1} that may also be attributed to MgO. However, the low signal/noise ratio impedes the exact assignment of these vibrational modes. Although XRD and FTIR techniques do not allow detection of the NiAl_2O_4 spinel phase, in the present case, the aforesaid spinel structure depicts Raman bands at approximately 200 , 370 and 612 cm^{-1} , in line with an earlier report [31]. These Raman bands appear to be superimposed with those of the NiO, MgAl_2O_4 , MgO and Co_3O_4 phases and thus the presence of the spinel structure cannot be ruled out. When comparing the Raman spectra of the supported samples, no distinct changes in the spectra are observed compared to the unsupported solids.

Summarizing, XRD, FTIR and Raman measurements demonstrate either good dispersion of Ni and Co nanoparticles or their interactions with supports, as further seen by textural and morphological properties.

2.2. Textural and Morphological Properties

The textural properties of the solids are examined via N_2 physisorption isotherms and the corresponding pore size distributions (Figure 4). As expected, the isotherms exhibit a hysteresis loop at high relative p/p_0 values indicating a type IV isotherm, as defined by the IUPAC classification [13,30,37]. Such features suggest that the sol-gel method leads to the presence of uniform mesopores arrangements. The porosity of the unsupported solids is evident by their large nitrogen adsorption uptake at saturation, which has a hysteresis very similar to the H₄ and H₁ types (Figure 4A₁). In other words, LA and ZA supports are formed by particles crossed by nearly cylindrical channels or agglomerates of particles [38,39], as further seen by SEM-EDS analyses.

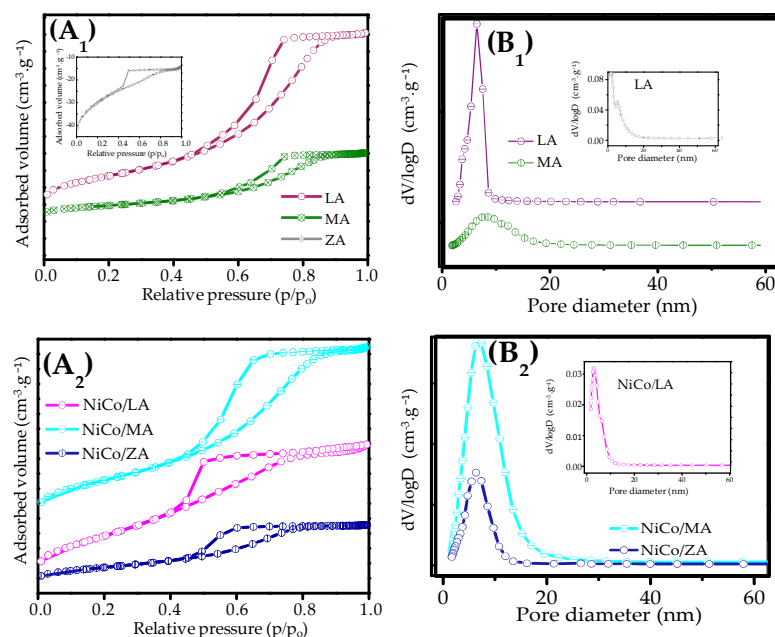


Figure 4. (A) N_2 physisorption analyses and the corresponding (B) pore size distributions of the supported and unsupported solids. The inset figure (A₁) is the isotherm of the ZA sample, whereas insets (B₁, B₂) are the pore size distribution curves of ZA and NiCo/LA samples, respectively. The figure (A₂) corresponds to the isotherms of the supported solids.

Regarding the MA support, a steady rise in p/p_0 in the range of 0.1–0.6 is followed by a gradual increase in nitrogen uptake till the saturated adsorption plateau at p/p_0 values is nearly 1. This is likely because of the capillary condensation phenomena in mesopores larger than 4 nm [39].

The textural properties of the solids are presented in Table 1. The BET surface area of the γ -Al₂O₃ sample is 182 m²·g⁻¹, with a pore volume of 0.29 cm³·g⁻¹, which confirms that the sol–gel method is efficient to obtain porous metal oxides [13,21,35]. The BET surface area of unsupported LA is nearly 3 folds higher than that of bare γ -Al₂O₃ with similar trends followed by the pore volume. The textural properties differ significantly with ZA and MA supports having lower surface areas and pore volumes compared with LA and γ -Al₂O₃ counterparts as well (Table 1). In this regard, the expansion of the alumina lattice due to La³⁺ cations seems to be well in agreement with the highest textural parameters of the LA sample. Meanwhile, the lattice contraction with smaller cations such as Mg²⁺ and Zn²⁺ accounts for the lower textural parameters of MA and ZA.

Table 1. Textural properties of the solids in study.

Samples	Surface Area (m ² g ⁻¹)			^d Mesopore Volume (cm ³ g ⁻¹)		^e Total Pore Volume (cm ³ g ⁻¹)	^f Pore Diameter (nm)
	^a BET	^b External	^c <i>t</i> -Plot				
γ -Al ₂ O ₃	182	87	23	0.29	0.29		6.1
LA	476	445	31	0.85	0.86		6.7
MA	162	152	9	0.30	0.31		7.5
ZA	109	82	27	0.04	0.05		3.1
NiCo/LA	148	152	0	0.20	0.20		4.1
NiCo/MA	130	125	5	0.17	0.17		5.6
NiCo/ZA	50	48	1	0.08	0.15		5.0

^a Brunauer–Emmett–Teller surface areas. ^b External surface area obtained from *t*-plot method. ^c Micropore surface area obtained by the *t*-plot method. ^d Mesopore volume and ^e Total pore volume taken by Barrett–Joyner–Halenda method. ^f Adsorption average pore diameter derived from Barrett–Joyner–Halenda method (4 V/A).

This clearly illustrates the rapid diffusion of divalent cations to be included in the alumina framework during the peptization and co-condensation steps that occurred in the synthesis, besides alumina avoiding the particle coarsening, as shown by earlier reports [13,37,38].

It is worth to note that the micropores volumes of the unsupported solids have quite similar values, all being much lower than the total pore volumes, which confirms the supports are mesoporous. In addition, the *t*-plot surface areas for micropores are much lower than the mesoporous parameters suggesting a marginal microporous contribution from binary solids LA and MA (Table 1). Additionally, the external surface areas corresponding to the mesopores and macropores and yet the crystal void spaces in pore structures are listed in Table 1. The ZA support holds the lowest external surface area evidencing the presence of micro and meso porosity, while other solids have mainly mesoporous structures. Meanwhile, the corresponding pore size curves (Figure 4(B₁)) show a monomodal distribution of pore diameters centered between 3.1 and 7.5 nm (Table 1), which confirms the prevalence of the mesoporous structure in the unsupported samples. Despite ZA has the lowest textural parameters among the unsupported samples, the average pore diameter of ca. 3.1 nm confirms the mesopore structure (Figure 4(A₁) inset) along with some micropores (Figure 4(B₁) inset).

The isotherms of the supported samples have similar features to the unsupported solids, e.g., type IV isotherms, although H₁ and H₂ hysteresis loops are observed (Figure 4(B₁)).

In addition, an unavoidable decrease in surface areas and the same, if not slightly lower, pore volumes are observed compared with the unsupported solids (Table 1). These evident changes are illustrated by the BET surface areas of NiCo/MA and NiCo/ZA, which drop strikingly by approximately 15% comparable to their supports, along with the total pore volumes declining to well below 20%. These results can be attributed to the cooperative interactions between the metal oxides dispersed on alumina-based solids by reducing the surface areas and pore volumes during the consecutive steps of calcination of

the supported solids. Such effects also result in the enlargement of the surface coverage, as shown by the external area values of supported solids, in general, being lower than those of unsupported solids. Remarkably, micropore areas and mesopore volumes decrease are a result of the absence of pore blockage by Ni and Co nanoparticles, as later seen by TEM. The NiCo/ZA is an exception, since the micropore volume augment suggests the smaller mesopores transformation into micropores upon dispersion of the metal oxides followed by two consecutive calcination steps of the sample. Correspondingly, a steep nitrogen uptake in NiCo/ZA at low relative pressure regions suggests the occurrence of some micropores, whereas the extent of adsorption in micropores partially disappears in NiCo/LA and NiCo/MA. The pore size distribution curves broadened and mean pore diameters range from 4.1 to 5.6 nm, compared with the unsupported solids. For instance, the pore diameter of NiCo/LA is ca. 4.1 nm appearing slightly smaller compared to those of NiCo/ZA and NiCo/MA. This closure of the pores of the former sample can be a result of the preferential deposition of the metal oxide particles in the mesopores or micro macropores with little effect coming from the Ni and Co nanoparticle sintering phenomenon.

The high porosity of the solids is consistent with the expected features for sol-gel based-solids. It is clear that the alumina support restrains the growth of metal oxide nanoparticles in the supported solids owing to the strong metal-support interaction.

In addition, the obtained values are all close to the nominal content of 1.0 wt.%, which suggests the samples successfully synthesized.

The transmission electron microscopy images depict the structural features of the supports (Figure 5). It is evident from the top of Figure 5(A₁) that LA consists of disordered particles, most of them agglomerated. The included Figure 5A₁ shows that these particles are 1–10 nm in size. Furthermore, the clear amorphous regions along with crystalline regions (square area in Figure 5(A₂)) generally show the features observed in the γ -Al₂O₃-based samples [21,22]. The arrow in Figure 5(A₃) depicts a border between two regions suggesting the grain boundary. The HRTEM image suggests lattice spacings of ca. 0.280 and 0.456 nm, which are indexed to be in the (022) and (111) planes of γ -Al₂O₃, as found elsewhere [40,41]. Additionally, inset Figure 5(A₃) illustrated a dark particle too large to be discerned, suggesting segregation of La₂O₃, in agreement with EDS results (Figure S1 in Supplementary Materials). In case of the MA support, similar particle agglomeration is seen in the low magnification TEM image with particle sizes of approximately 16 nm (Figure 5(B₁)). In the same vein, the crystalline regions appear evidently more than the LA counterparts (highlighted square and spherical regions in Figure 5(B₂)) but differ only in discontinuity of the pattern. This is indeed due to the superposition of the formed phases. The XRD and Raman results indicate supportive evidences for the MgO and MgAl₂O₄ formation, in agreement with Figure 5(B₃) through their lattice fringes.

Interestingly, ZA is composed of smaller particles with diameters within the range 1–7 nm being less agglomerated than those of LA and MA (Figure 5(C₁)). Besides, crystalline domains are also found with a d-spacing of ca. 0.247 nm (Figure 5(C₂)), which is associated with the (101) for cubic ZnO [42]. Moreover, the d-spacing of ca.0.280 nm (022) is associated with the γ -Al₂O₃ besides the presence of amorphous regions (the inset of Figure 5(C₂)). In addition, the particles of the binary ZA support appear to be significantly crystalline to generate the lattice fringes (Figure 5(C₃)) as those of MA.

Further information on the structural features of the supported samples is obtained by direct imaging of the structure through TEM. After dispersing the Ni and Co on LA, particles remain disordered with some degree of agglomeration (Figure 6(A₁)). This is in line with EDS results in Figure S2 in Supplementary Materials. The magnified trapeze highlighted area illustrates that the rippled aggregated particles contain notable nanoparticles dispersed on it (top left, Figure 6(A₁)). In these aggregates, the presence of lattice fringes indicates the crystalline domains of NiCo/LA (top middle, Figure 6(A₂)).

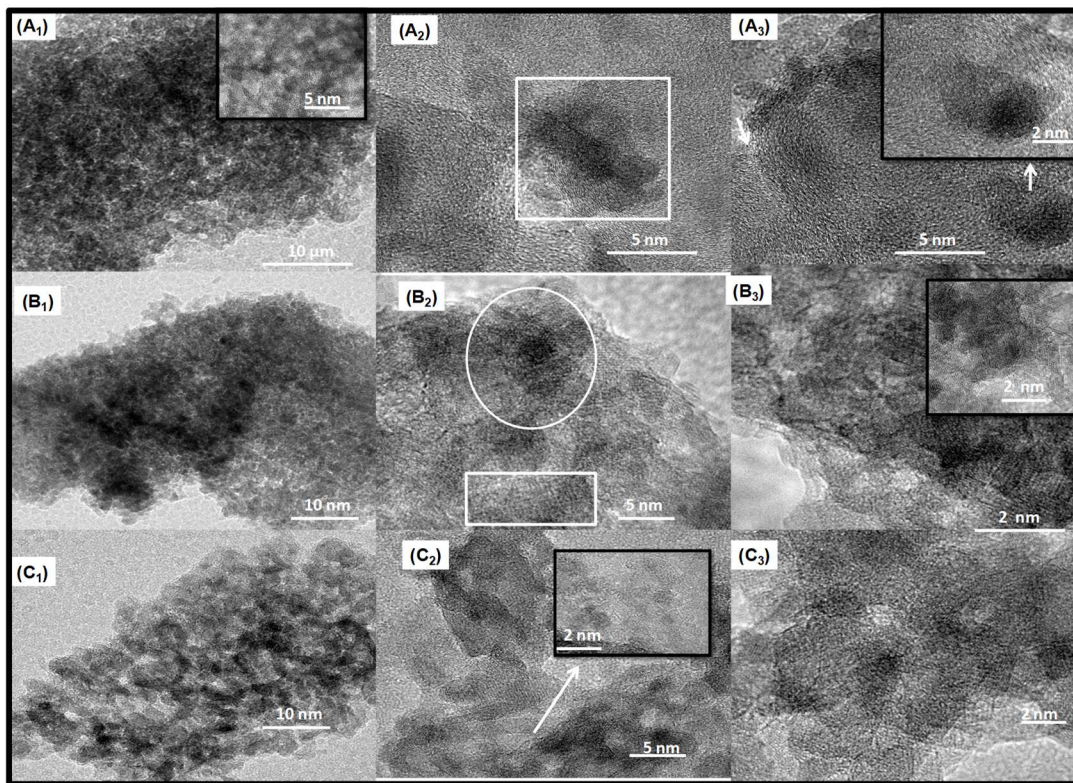


Figure 5. TEM images of the supports: (A) LA, (B) MA and (C) ZA samples. Insets illustrate parts of the figure at higher magnifications.

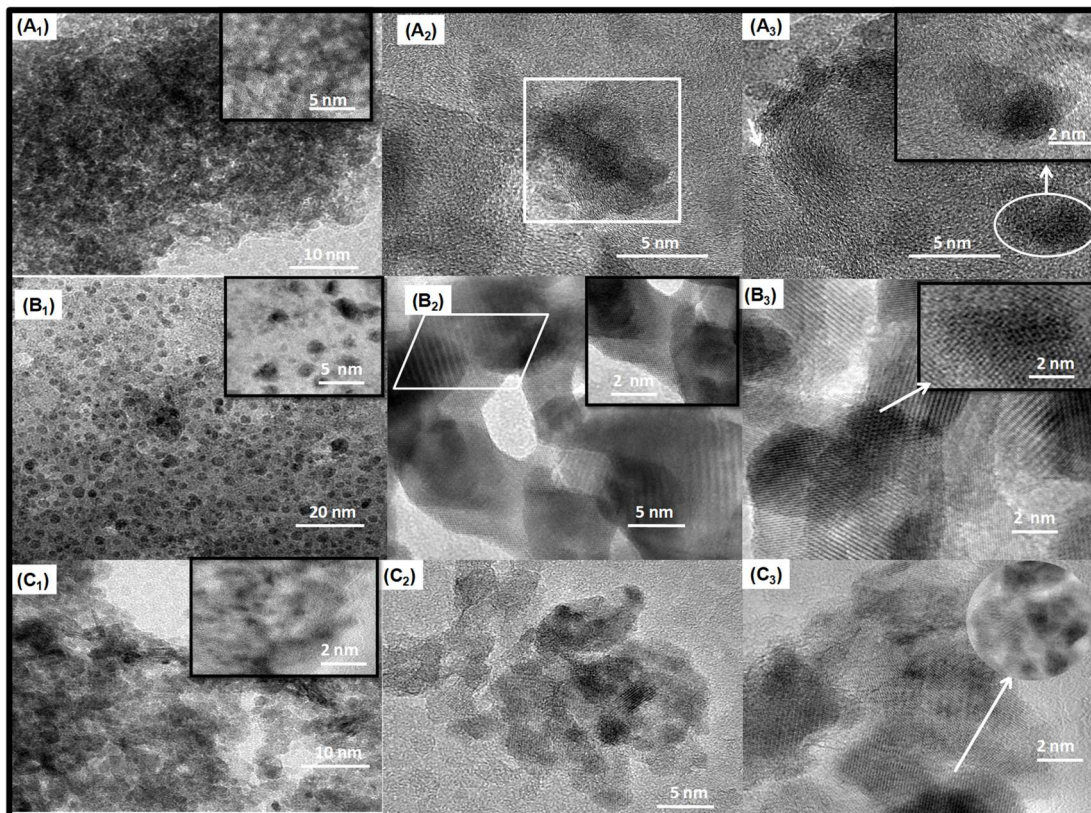


Figure 6. TEM images of the supported samples: (A) NiCo/LA, (B) NiCo/MA and (C) NiCo/ZA samples. Insets illustrate parts of the figure at higher magnifications.

The included high magnification image shows particle intergrowth predominantly appearing in the crystalline regions (top middle, inset Figure 6(A₂)). The periodic planes correspond to the d-spacing of 0.280, 0.290 and 0.241 nm with (022), (220) and (111) lines, respectively. These planes are indicative of a regular arrangement of γ -Al₂O₃, spinel Co₃O₄ and cubic NiO, in agreement with the findings [41,43]. The nanoparticles have somewhat small sizes ranging from 1 to 5 nm, being finely dispersed throughout the bulk (top right, Figure 6(A₃)) some of them included in the large pores of the sample, as shown by the selected area (inset top right, Figure 6(A₃)).

This is well-matched with the textural properties that depict a large surface area of ca. 400 m² g⁻¹ for NiCo/LA and graded meso and macroporosity. Comparatively, well-dispersed NiO or Co₃O₄ nanoparticles are clearly visible in the low magnification TEM image of NiCo/MA with a higher dispersion of these entities, e.g., more than 83.2% detected for NiCo/MA (center right, Figure 6(B₁)) against 21% for NiCo/LA. Thus, there is an obvious uniform distribution of the nanoparticles on the surface of MA support with sizes extending from 1 to 13 nm (inset, Figure 6(B₁)). Evidence for the porosity of the MA support through the mesoporous and macroporous structure is given in Figure 6(B₂), top middle. An illustrative example of interparticle growth is shown by the highlighted trapeze, which is amplified in the inset of Figure 6(B₂). Importantly, the lattice spacings of 0.280 (022), 0.290 (220), 0.241 (111), 0.210 (200) and 0.281 nm (103) correspond to the Co₃O₄, NiO, Al₂O₃, MgO and MgAl₂O₄, respectively. Furthermore, NiCo/ZA exhibits a platelet of particles (top bottom, Figure 6(C₁)) with a uniform distribution compared to NiCo/LA. From the magnified image, the smaller particles are arranged in a perfect manner inside the crystalline ZA support (inset, Figure 6(C₁)). The sizes of NiO and Co₃O₄ nanoparticles are within 5–19 nm range, which is slightly lower than those of NiCo/LA. The high magnification image in the bottom center of Figure 6(C₂) shows a well-organized lattice arrangement of crystalline Al₂O₃, Co₃O₄ and NiO and a d-spacing of ca. 0.247 nm (101) is attributed to cubic ZnO. Figure 6(C₃) illustrates the regular porous structure along with the crystalline structure of the particles by the lattice fringes. Additionally, the magnified view of the figure depicts the presence of some nanoparticles inside the pores (inset of Figure 6(C₃)).

2.3. Acidity of the Catalysts

Acidity is measured by NH₃-TPD and the results are summarized in Table 2. A theoretically confirmed rule illustrates that at temperatures lower than 250 °C, the acid sites measured by NH₃-TPD are of weak strength, whereas those of medium strength retain ammonia showing desorption peaks close to the 250–350 °C range [13,28,44]. On the contrary, the characteristic acid sites having strong strength present broad peaks located at 500–700 °C range [13,44]. The NH₃-TPD curves of the pure alumina sample comprise peaks located at 150–250 °C corresponding to the acid of weak acidity and those of medium strengths in the 250–400 °C range (Table 2), in very close agreement with the findings [13,43]. Hence, the γ -Al₂O₃ sample displays a total acidity of ca. 0.187 mmol·NH₃·g⁻¹ [13]. These acid sites are positioned below 300 °C, being associated with Lewis acid sites whilst the high temperature desorption peaks superior to 500 °C is attributable to either solely Brønsted acid sites or both Brønsted and Lewis acid sites [28,45].

With the addition of the basic promoters to the alumina, the sol-gel prepared binary support oxides decrease their amounts of surface acid sites, prevailing very few weak to medium acid sites. Based on the reports, MgO, ZnO and La₂O₃ are assumed to be basic oxides and therefore, the absence of acid sites is not expected [41–44,46]. In contrast, alumina itself has both acid and base sites characteristic of an amphoteric oxide [42,44]. At the opposite, the acidity can be tuned by altering the alumina chemical composition through doping, and yet aluminas are a typical solid base, when promoted by alkali-metals, alkali-fluorides, alkali-amides, and/or alkali-hydroxide forming as super or strong base catalysts [42,44].

Table 2. Acidity measurements by NH₃-TPD of the solids. The amount of ammonia desorbed per gram of catalyst was obtained from the temperature ranges to calculate the total concentration of acid sites.

Catalyst	Acid Amount mmol NH ₃ g _{cat} ⁻¹ at 150–250 °C	Acid Amount mmol NH ₃ g _{cat} ⁻¹ at 250–400 °C	Acid Amount mmol NH ₃ g _{cat} ⁻¹ at T > 500 °C	Total Amount mmol NH ₃ g _{cat} ⁻¹
NiCo/MA	0.13	0.10	0.02	0.25
NiCo/LA	0.14	0.12	-	0.26
NiCo/ZA	0.07	0.11	0.01	0.19

Thus, the acidity of the supports is adjustable depending on the promoter added. For instance, the Zn addition on alumina gives a considerable drop in total acidity to 0.19 mmol·NH₃·g⁻¹ while the modification by Mg increases the total acidity to 0.25 mmol·NH₃·g⁻¹ and the addition of La slightly increases the total acidity to 0.26 mmol·NH₃·g⁻¹. Upon examination of the strength distributions, almost all samples appear in regions of weak to mild acidity with the absence of acid sites of strong strength, as expected [28,45]. Furthermore, the amount of acid sites for the supported samples has distinctive shifts for higher temperatures owing to the NiO and Co₃O₄ phases dispersed on the supports, making the total acidity considerably higher than that of γ-Al₂O₃, except for NiCo/ZA. Remarkably, the good dispersion of NiCo on the supports provides an evident enhancement of acid sites strengths with similarity in terms of distributions, in spite of large differences in surface acidity due to Ni and Co acting as Lewis acid sites. Therefore, the supported solids have much higher total acidity values than the unsupported ones, following the order: NiCo/LA ≅ NiCo/MA > NiCo/ZA.

All these properties suggest that the promoters are included in the alumina structure, modulating its textural properties, morphology and acidity to favor the interaction of Ni and Co in close contact with the support. This will result in a much high number of active sites possessing weak to mild acidity for promoting AG reaction, as further shown.

2.4. Electronic Properties and Surface Compositional Characterizations

In an attempt to further characterize the valence states and the presence of possible defects in the supported solids, EPR measurements are performed. As expected, γ-Al₂O₃ does not exhibit EPR signals owing to the absence of paramagnetic impurities, as found elsewhere [47]. On the contrary, the EPR spectra of the supported solids depict asymmetric resonance signals in two distinct regions (Figure 7a). At the magnetic field, the strong resonance located in the 2400–5000 G range is attributable to the paramagnetic Ni²⁺ species from the small NiO particles [48,49]. The *g* value close to 2.2 is assigned to either small ferromagnetic Ni clusters or the substitutional cubic Ni²⁺ ions in oxides matrix [48,49]. These Ni²⁺ species in such a low NiO amount on the surface could be strongly interacting with the alumina, as further demonstrated by the XPS results.

It is noteworthy that the asymmetrical peak in the 2400–5000 G range is superimposed on a broad anisotropic peak with a *g* value of 2.10, which is attributed to Co²⁺ ions from Co₃O₄ [50]. This result agrees with the TEM analyses that demonstrate the presence of the spinel phase in all the solids. According to the findings, the *g* value of ca. 2.00–2.12 can also be attributed to the electrons trapped by oxygen vacancies [29]. This also indicates that the samples have the oxygen atoms at the surface appearing to be interacting with the vacancies and these oxygen species could mask their own vacancies present or even interact with them, generating the ferromagnetic signals at 2900 G [51].

Additionally, it cannot be excluded the Mg, La and Zn species incorporated in the alumina structure contribute to some extent to the background of the EPR spectra. However, the supported samples have similar EPR curves, independently of the MA, LA and MA support and thereby the influence of the aforesaid ions is not detectable because of their low concentrations or masking under the EPR spectra of the Ni and Co species.

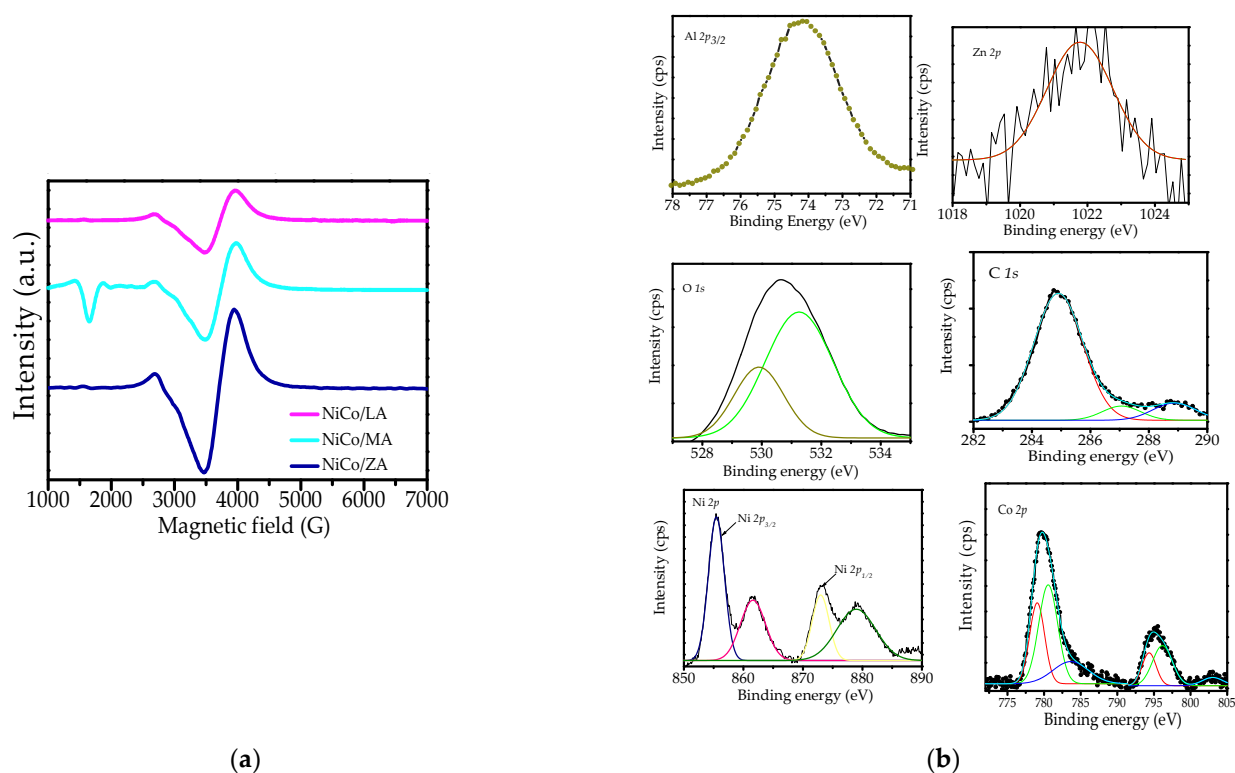


Figure 7. (a) EPR measurements for supported solids (b) Representative XPS spectra for the NiCo/ZA supported solid.

The chemical states and surface compositions of the supported solids are evaluated by XPS analyses. A full scan range XPS survey spectrum depicts the presence of the Al $2p$, Zn $2p$, O $1s$, C $1s$, Ni $2p$, and Co $2p$ signals for the NiCo/ZA sample (Figure 7b). Besides the aforesaid elements, the XPS spectra of NiCo/MA and NiCo/LA samples have additional Mg $1s$ and La $3d_{5/2}$ core levels signals. For all samples, the dominant peak at 73.8–74.1 eV is assigned to Al $2p$ signal (Table 3). This suggests the presence of Al(III) in Al–O and Al–OH bonds on the solid surface existing purely in the form of γ -Al $_2$ O $_3$, in agreement with the findings [2]. To prove that the binary oxides supports are formed, the Zn $2p_{3/2}$ core level spectrum appears in NiCo/ZA as a very weak fitted peak (Figure 7b) corresponding to Zn (II) species from ZnO [52]. It is worth noting that the surface Zn content is quite low ca. 0.46 wt.% whereas the Al content is 28.59 wt.%, which suggests that most of ZnO oxide is on the bulk forming ZnO–Al $_2$ O $_3$ support. This result agrees with the XRD, Raman and TEM results that indicate the existence of the ZnO–Al $_2$ O $_3$ binary support. In the case of NiCo/LA, the high resolution La $3d_{5/2}$ core level spectrum reveals an intense characteristic peak that emerges at 834.9 eV matching well with La(III) from La $_2$ O $_3$ [21]. Moreover, the surface La content is 0.39 wt.% with respect to that of 25.66 wt.% of Al, which indicates that lanthanum is mostly included in the bulk of La $_2$ O $_3$ –Al $_2$ O $_3$ support. For NiCo/MA, the peak of Mg $1s$ core level occurred at 1303.4 eV, which stands for the Mg(II) from MgAl $_2$ O $_4$ and MgO phases [29].

A relatively small amount of Mg of approximately 0.35 wt.% is detected together with 22.44 wt.% of Al because of the formation of bulk phase. This is in line with the XRD results that suggest the presence of these phases besides alumina. Based on the fact that the Mg, Zn and La contents in the bulk are 12.0 wt.% each, it can be inferred that the surface contributions of these species are too low being these species mostly included in the bulk. In addition, the curve fitting of the high resolution C $1s$ core level spectrum shows three contributions in all solids, with binding energies values of 284.8, 286.8 and 288.9 eV, which are assigned to adventitious carbon/C–C/–C=C– bonds, C–OH bonds and C=O bonds,

respectively [2,21]. These carbon species arise probably due to the presence of some organic contaminants adsorbed on solid surfaces being in small amount of ca. 6–7 wt.%.

Table 3. Binding energies values (eV) and Ni/Al and Co/Al ratios obtained from XPS spectra of the supported samples.

Sample	Al 2p	Mg 1s	Zn 2p _{3/2}	La 3d _{5/2}	C 1s	Co 2p _{3/2}	Ni 2p _{3/2}	O 1s	Ni/Al	Co/Al	
NiCo/LA	73.8	-	-	834.9	284.9	780.3	855.6	530.6	0.44	0.57	
					286.9		795.0				531.2
					288.9		802.3				
							872.6				
							878.2				
NiCo/MA	74.2	1303.4	-	-	284.7	780.6	855.8	530.4	0.78	0.45	
					286.8		795.1				531.3
					288.8		802.4				
							872.3				
							878.5				
NiCo/ZA	74.1	-	1022.1	-	284.8	780.2	855.4	530.4	0.31	0.47	
					286.4		795.0				531.0
					288.7		802.3				
							872.5				
							878.8				

The analysis of the high resolution O 1s core level spectrum illustrates two distinguished oxygen species, including 530.6 and 531.3 eV, which is consistent with the chemisorbed surface oxygen and water surface adsorbed OH and/or oxygen vacancy and lattice O²⁻ species in Me-O bonds [2,21,52]. Indeed, the bulk oxygen species possessing a binding energy of 530.6 eV is accompanied by hydroxyl groups with a binding energy of 532.3 eV with a relatively high amount for NiCo/ZA whereas NiCo/LA and NiCo/MA have minor amounts. Thus, NiCo/MA holds the most oxygen vacancies among these solids, which is consistent with the abundant oxygen vacancies found by the EPR results.

The high resolution Co 2p spectrum is deconvoluted into two contributions with binding energies at 780.3 and 795.0 eV, which are associated with the doublet Co 2p_{3/2}-Co 2p_{1/2}. In addition, a weak satellite at approximately 802.1 eV appears in all spectra. The peaks at 780.3 and 795.0 eV are ascribed to the simultaneous presence of Co(III) and Co(II) from Co₃O₄ on the solid surface [22,52]. The EDS analyses found a large amount of Co species on the solid surface. The findings state that the absence of strong shake-up satellites could be associated with the presence of Co₃O₄ [36,52]. The Co/Al ratio is calculated to be 0.57, 0.45 and 0.47 for NiCo/ZA, NiCo/MA and NiCo/LA, suggesting a lower amount of these species on the latter solids. The doublet Ni 2p_{3/2}-Ni 2p_{1/2} appears at 855.6 and 878.2 eV and two shake up satellites at 861.1 and 872.6 eV for NiCo/LA (Table 3). The Ni 2p spectra for samples NiCo/LA for NiCo/MA have similar binding energy values. These components are attributed to Ni(II) from surface NiO [22,52]. The Ni/Al ratios are 0.44, 0.78 and 0.31 for NiCo/LA, NiCo/MA and NiCo/ZA, respectively. This suggests a higher coverage of the NiCo/MA surface by the NiO, as observed by the TEM measurements and EDS analyses (Supplementary Materials).

2.5. Catalytic Performance in EG Reaction

The esterification of glycerol in the presence of acetic acid is conducted to evaluate the catalytic properties of the solids. In preliminary investigations, the reaction is carried out in the presence of various catalysts (Table 4). It is notable that the glycerol conversions on unsupported solids are too low with MA holding a conversion of 4.5%, while those of ZA and LA are just 3.6 and 2.3%, respectively.

Table 4. Glycerol conversions, reaction rates and product selectivities for the catalysts evaluated in 1h of EG reaction. Reaction conditions: glycerol to acetic acid (molar ratio) = 1:3, reaction temperature = 80 °C, catalyst mass = 0.50 g.

Catalysts	X (%)	Rate (mmol _{gly} g ⁻¹ cat h ⁻¹)	Selectivity (%)		
			Monoacetin	Diacetin	Triacetin
Blank	1.7	0.01	-	-	-
MA	4.5	0.05	-	9.0	23.0
ZA	3.6	0.04	-	12.0	12.1
LA	2.3	0.02	-	15.0	17.4
NiCo/MA	11.0	0.31	-	7	18.0
NiCo/LA	7.0	0.17	-	-	14.0
NiCo/ZA	5.0	0.14	-	-	16.0
^a γ -Al ₂ O ₃	80	0.80	84	10	0.8

^a Reaction conditions: glycerol/acetic acid (molar ratio) = 1:9, reaction temperature = 100 °C, reaction time = 6 h, catalyst weight = 0.50 g.

On the other hand, glycerol conversion on γ -Al₂O₃ is higher than those of the most active binary supports. The acidity of the alumina decreases significantly upon incorporating the basic promoters appearing to be, at first sight, disadvantageous to convert glycerol. As shown previously, alumina possesses acid sites of weak to medium strength [13]. Hence, it is expectable that conversions and selectivities would be high under the very mild reaction conditions tested. However, alumina catalyst requires high temperature, e.g., 100 °C and long reaction times, e.g., 6 h to transform glycerol, besides the selectivity of the triacetin is very poor. Importantly, a NiCo/Al₂O₃ sample prepared in this study has similar conversion and selectivity within 1h comparing with γ -Al₂O₃, but Ni and Co leaching over the course of the reaction deactivated the solid. Particularly, studies on EG reaction using basic promoters added to alumina, for example, CaO and MgO as well as Ni or Co addition to Al-based catalysts with different metal loadings have shown substantially lower activities than the those of the supported catalysts in the present work [53–56]. This is due to the low water tolerance of the catalysts during the esterification of glycerol causing the deactivation of the solids over the course of the reaction.

According to mechanistic considerations [12], the EG reaction with acetic acid involves the protonation of the carbonyl group of the acetic acid molecule over Brønsted acid catalysts possessing strong strengths [5]. Subsequently, the activated carbonyl group formed in the previous step reacts with a hydroxyl group of glycerol through nucleophilic attack to give an intermediate C–O bond [5,12]. The reaction proceeds via the loss of a water molecule from the intermediate and the acetin isomers formation, e.g., 1-monoacetin and 2-monoacetin [2,5]. The serial mechanism of monoacetins reaction and acetic acid molecules results in diacetins, e.g., 1,2-diacetin and 1,3-diacetin, and further reaction of these latter molecules with acetic acid produces triacetin [1–5,53].

One thing that deserves to be mentioned is that the initial ratios somehow achieve better values for the supported solids (Table 4) compared to those of the unsupported catalysts due to the low amount of acid sites present in the latter (Table 2). In the case of supported solids, glycerol conversions are also similar in terms of the trends for the kind of support with slightly higher values than those of binary catalysts. Such an effect is found prevalently with the presence of Ni and Co nanoparticle dispersed on the supports, since the nanoparticles themselves exert a dual role of chemisorb glycerol and work synergistically with basic promoters to adsorb acetic acid. This would influence the catalytic performance to some degree. In these systems, the nanoparticles dispersed on the supports are not affected by the water formation that leads to the common acid sites deactivation during the EG reaction, as found elsewhere [5,9]. Selectivities to triacetin do not change significantly over the supported solids whilst mono and diacetin are not produced. This is due to the large amount of by-products observed, after conducting the reaction in the harsh reaction conditions shown in Table 4.

Further studies on the activity of solids on supported solids are being carried out to examine the effects of the structure on their catalytic performances. Figure 8A clearly depicts a gradual increase in the glycerol conversion with increasing reaction time for supported catalysts. Such an effect is generally ascribed to the concentrations of the components being far from equilibrium at the initial stages of the reaction and then, the system approaches equilibrium with the progress of the reaction. The trend of the activities summarized in Figure 8A shows that the binary supports contribute to convert glycerol with conversions greater than 11% in short times. Raising reaction times within 4 h gives stable conversion of NiCo/ZA, while NiCo/LA conversion slightly increased. This may cause aggregation of the support particles and, subsequently, a lower stability of the catalyst up to 4 h, as shown later in the recyclability experiments. Notably, NiCo/MA also exhibits a large boost at longer reaction times and still maintains more than 28% glycerol conversion after 6 h owing to the solid possessing plenty of acid sites and existence of more exposed Ni and Co sites on the support surface, resulting in a high availability of the active sites to enhance the catalytic performance. Thus, Ni and Co nanoparticles dispersion on MA and the low acidity and probably also to its synergistic effect may contribute to the catalytic activity of the solid. Additionally, the better catalytic performance of NiCo/MA may be due to the porosity.

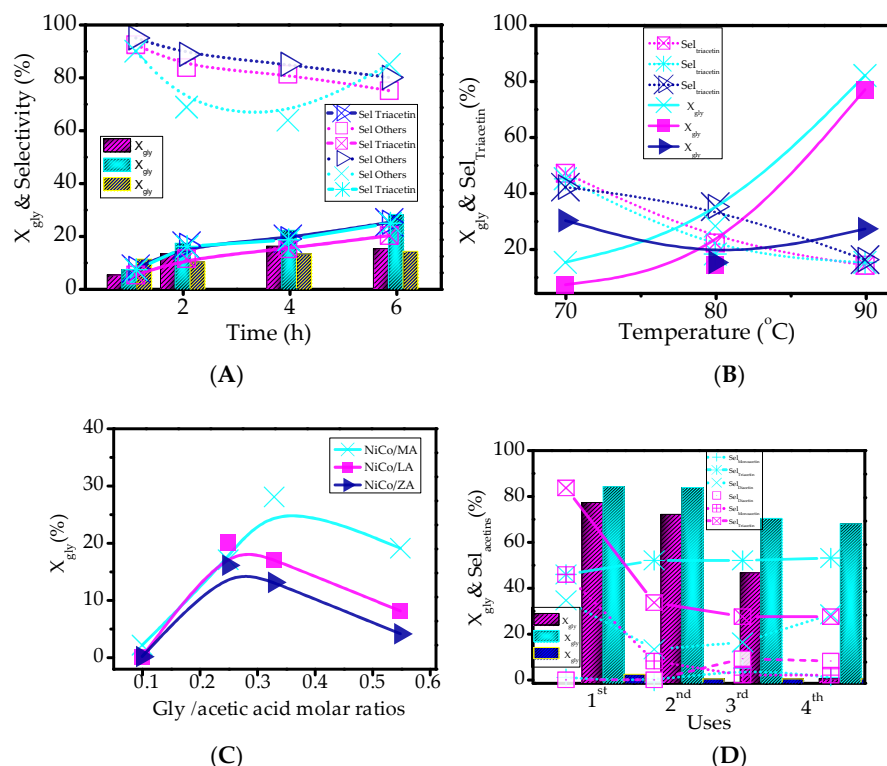


Figure 8. (A) Catalytic activity tests in the EG reaction as a function of the reaction time. Reaction conditions: glycerol to acetic acid (molar ratio) = 0.33, reaction temperature = 80 °C, catalyst mass = 0.50 g. The symbols for (■ * ×) NiCo/MA, (■ □ □) NiCo/LA and (■ × △) NiCo/ZA samples represent glycerol conversions, selectivity to triacetin and selectivity to others by-products. (B) Influence of the temperature on the catalytic properties of the samples. The symbols for (■ * ×) NiCo/MA, (■ □ □) NiCo/LA and (■ × △) NiCo/ZA samples represented glycerol conversions and selectivity to triacetin taken in 6 h of reaction. (C) Glycerol to acetic acid molar ratios studied at 80 °C using a catalyst mass of 0.50 g in 6 h of reaction. (D) Reusability studies. Reaction conditions: glycerol to acetic acid (molar ratio) = 0.33, reaction temperature = 80 °C, catalyst mass = 0.50 g for each cycle of 24 h. The symbols for (■ □ □) NiCo/LA (■ * × +) and NiCo/MA samples represent glycerol conversions, selectivity to triacetin, diacetin and monoacetin.

In spite of the high porosity of NiCo/LA in comparison to NiCo/ZA and NiCo/MA, the catalytic performance of the former is attributable to the low interaction between Ni and Co nanoparticles and the LA support. This facilitates the leaching of the particles during the reaction, thereby causing loss of activity after 6 h, as demonstrated by the observed tendency to activity decay (Figure 8A). For NiCo/ZA possessing lower acidity, the deactivation of the acid sites by water is possibly the reason why the solid exhibit lower glycerol conversion compared with NiCo/MA. Moreover, the selectivities to triacetin increases as the reaction proceeds, but it hardly changes within 6 h for all solids (Figure 8A). Contrary, selectivities to other by-products significantly enhanced during the whole time intervals reaching values nearly 70% in 6 h due to the triacetin oligomers formation, namely other by-products (Figure 8A).

Figure 8B illustrates the dependence of the temperature of glycerol conversion and selectivity to triacetin. The catalysts show a glycerol conversion initially below 10% at 70 °C, reflecting the need for heating to enhance catalytic performance. The evolution of the glycerol conversion at temperature of 80 °C shows an increment in activities due to the effect of the furnishment of heat to the reaction [54,56]. For NiCo/ZA, a sudden decrease of glycerol conversion suggests that by-products are formed, while the oligomers are irreversibly adsorbed to the active sites at 90 °C achieving 27% of conversion and 16% of triacetin selectivity (Figure 8B). Such temperature effects are typical of the drop in glycerol conversion with rising temperature due to the overall exothermicity of the reaction [12]. In contrast, the glycerol conversion behaviors of the NiCo/MA and NiCo/LA samples are apparently different from that of NiCo/ZA. For instance, the glycerol conversion of NiCo/MA and NiCo/LA is found to be ca. 3 times greater than that of NiCo/ZA at 90 °C (Figure 8B). That is, the conversion of glycerol of NiCo/ZA remains almost constant in the temperature range investigated. In that case, the temperature causes variations of the specific heats, when the hydroxyl group of glycerol is substituted by acetyl groups from acetic acid until reaching a plateau [12]. The calculated energy of activation for NiCo/MA, assuming pseudo-second-order dependence on glycerol concentration, is found to be 18.0 kJ mol⁻¹, which is lower to that observed for sulfated alumina e.g., 70 kJ mol⁻¹ [54].

In addition, the results indicate a trivial decrease in monoacetin and diacetin selectivities with the rising temperature and thus the catalysts offer high selectivity for triacetin and by-products in the range of the studied temperature (Figure 8B). The conversions steeply increase for NiCo/MA and NiCo/LA over the entire temperature range evaluated and selectivities to triacetin finally approach low values due to the oligomers production at high temperatures. Accordingly, increasing the temperature from 70 to 90 °C results in a decay in selectivity to triacetin from 47% to 13% on all solids. These results are hardly confirmed by the fact that the furnishment of heat to the system contributes to the esterification of monoacetin to triacetin as this reaction is a highly endothermic process [12]. In contrast, this effect is also observable for NiCo/MA, which reveals differences in acidity and porosity in comparison with those of the other samples, and thus, high temperatures improve the triacetin production.

Notably, samples possess remarkable catalytic performances at 80 °C and, thereby the catalytic activity studies are further continued at this selected temperature. The typical glycerol conversion curve dependence of the molar ratio is shown in Figure 8C. A considerable increase in the catalytic activity of the solids is found with increasing glycerol to acetic acid molar ratios from 0.10 to 0.33, providing a subsequent drop in glycerol conversion at glycerol to acetic acid molar ratio of 0.55 for all solids (Figure 8C). Reaction mixture containing high concentrations of viscous glycerol reactant, such as glycerol to acetic acid molar ratio of 0.55, limits the access of reactants to either active NiCo on the surface of the support or the acid sites of the support might be restricted. For instance, NiCo/MA seems to reach glycerol conversions of approximately 2 to 28%, when the molar ratio of glycerol to acetic acid is increased from 0.10 to 0.33 affording 16 and 22% of triacetin. A closer inspection of the behavior of NiCo/ZA shows evidence of obvious deactivation of the solid by leaching of the active sites, which nicely explains its poor catalytic activity

varying the molar ratios between glycerol and acetic acid. It is also apparent that increasing the molar ratios from 0.25 to 0.55, the glycerol conversions little decays from 20% to 8% over NiCo/LA. No obvious change in triacetin selectivity is shown over all supported solids with molar ratios above 0.55. In this sense, the findings illustrate that the modulation of the acidity and porosity of the catalysts has an important role in determining the efficiency of diffusion of reactants and products to achieve good selectivities to triacetin [3,5]. In view of these findings, triacetin possesses a molecular diameter of ca. 4.5 nm and thus, it requires space to diffuse into the catalyst pores and, if the active sites are on the surface, this is not a limiting factor for triacetin formation over the solids under investigation.

As the supported solids exhibit improved performance in terms of glycerol conversion and triacetin selectivity at the molar ratio of glycerol to acetic acid of 0.33 and temperature of 80 °C, reusability studies are conducted under optimized conditions for 1–4 cycles of uses of 24 h each. As described in Figure 8D, an activity loss of 8% from the 1st cycle to the 2nd cycle use is observable for NiCo/LA, possibly because of the simultaneous increase in the concentration of the by-products and leaching of the active sites. Accordingly, the values for the triacetin selectivity presented by NiCo/LA decline from 84% to 35%, whereas monoacetin and diacetin follow similar trends of decay. Amongst the catalysts tested herein, the NiCo/ZA appears to be less active and selective to acetins due to the inevitable nanoparticles leaching and strong by-products adsorption reaching complete deactivation especially in the first use. When the EG reaction lasted for 48 h, e.g., 2nd use, glycerol conversion of NiCo/LA reached a slightly continuous drop achieving glycerol conversion and monoacetin selectivity of 77 and 10%, respectively. Again, NiCo/MA appears to be very stable during repeated uses with glycerol conversions ranging between 84 and 70%, in the second and third cycles of uses. This could be an effect of the presence of the NiCo active sites helped by the stable spinel $MgAl_2O_4$ phase, acting as an additional active component to improve the catalytic performance. The production of the acetins consisting of ca. 53% of triacetin, 29% of diacetin and 4% of monoacetin besides 14% of by-products of its condensation, follows the same trends with quite constant glycerol conversions. When the reaction time is extended above 78 h in the fourth cycle, the glycerol conversion of NiCo/LA is null, considering the nanoparticles leaching as the most important deactivation factor for its poor reusability. After three repeated uses, NiCo/MA retains more than 67% of its initial activity with 53% of triacetin selectivity remaining in a state of slow down for another five cycles. Previous studies on EG reaction carried out with supported Ni and Co-based catalysts have demonstrated that the strong by-products adsorption thought to be mainly on the surface of the acidic sites of supporting oxides and the metal nanoparticles leaching are among the leading causes of catalyst deactivation [5].

From the obtained results, the activity of NiCo/MA is nicely preserved for up to four cycles of the reusability test and thereby, the solid is more resistant to deactivation compared with the other NiCo supported catalysts counterparts due to the intrinsic synergistic effect between support and nanoparticles. The presence of the stable spinel $MgAl_2O_4$ phase possessing lattice oxygen species acts as additional active component to improve the NiCo/MA activity and selectivity in the esterification of glycerol. The catalytic performances of the supported solids definitely demonstrate the crucial role of the structure, porosity, acidity of the catalysts in the activity.

3. Materials and Methods

3.1. Materials

Aluminum tri-sec-butoxide ($Al(O\text{-}sBu)_3$, 99%), ethanol (99.5%), lanthanum(III) nitrate hexahydrate ($La(NO_3)_3 \cdot 6H_2O$, 99.9%) magnesium(II) nitrate hexahydrate ($Mg(NO_3)_2 \cdot 6H_2O$), zinc(II) acetate dihydrate ($Zn(CH_3CO_2)_2 \cdot 2H_2O$), nickel(II) nitrate hexahydrate ($Ni(NO_3)_2 \cdot 6H_2O$) and cobalt(II) nitrate hexahydrate ($Co(NO_3)_2 \cdot 6H_2O$) were purchased from Sigma-Aldrich (Sigma-Aldrich, St. Louis, MO, USA). All chemicals were used as received without further purification.

3.2. Synthesis of the Alumina Support

The alumina support was synthesized by a sol-gel route based on previous studies [21,22]. Then, Co and Ni active components were dispersed on the support by the wet impregnation method. Approximately 103.5 mmol of aluminum tri-sec-butoxide and 3.25 mol of absolute ethanol were added to 4.2 mmol of lanthanum nitrate hexahydrate under stirring. Then, the formed suspension was refluxed for 1 h at 100 °C. Afterwards, a solution of nitric acid (0.05 mol·L⁻¹) was added dropwise into the previous mixture forming a slurry under continuous stirring. Then, the resulting mixture was kept again at 100 °C under reflux followed by stirring for 14 h. The pH of the medium was 5.0. Subsequently, the obtained gel was washed five times by centrifugation, before standing overnight. The xerogel was dried at room temperature for further calcination at 850 °C for 6 h under flowing air. The obtained solid was denoted as LA, representing the La₂O₃-Al₂O₃ support with 12.0 mol% of La.

In a similar procedure, the MgO-Al₂O₃ support was obtained by adding a desired amount of magnesium nitrate salt into the synthesis mixture. Briefly, 103.5 mmol of aluminum trisec-butoxide was dissolved into 3.25 mol of absolute ethanol for homogenization. The magnesium nitrate salt was then added to the suspension, which was immediately refluxed at 100 °C after adding the nitric acid solution. In the next step, the gel was washed, dried and calcined 850 °C to obtain the MA representing the MgO-Al₂O₃ support with 12.0 mol% of Mg. A summary of the preparation of the support is shown in Figure S3 in Supplementary Materials.

The ZnO-Al₂O₃ support was synthesized in a similar fashion as described above. In short, aluminum tri-sec-butoxide, absolute ethanol and zinc acetate were mixed simultaneously to the zinc acetate solution. Subsequently, the pH of the mixture was adjusted with the dropwise addition of nitric acid. After that, the mixture was refluxed at 100 °C for 14 h and calcined at 850 °C for 8 h. The support obtained was denoted as ZA referring to the ZnO-Al₂O₃ support with 12.0 mol% of Zn.

The incipient wetness impregnation method was used to prepare the NiCo catalysts supported on LA, ZA and MA (Figure S3b). Briefly, 1wt.% mmol of nickel nitrate aqueous solution was impregnated on 1 g of LA support in a rotatory evaporator at 70 °C for 2 h. After removing the excess solvent, the solid was dried at 120 °C and then calcined in air at 350 °C for 2 h. Another sequential step by impregnation 1wt.% of cobalt nitrate aqueous solution on the previous solid in a rotatory evaporator was performed. Afterwards, catalysts were dried overnight and calcined in air at 350 °C for 4 h. The resulting NiCo/La₂O₃-Al₂O₃ catalyst, namely NiCo/LA, had 1 wt.% of each metal.

For the preparation of the NiCo/MgO-Al₂O₃ and NiCo/ZnO-Al₂O₃, Ni and Co were introduced in two sequential steps of impregnation-evaporation methods similar to the abovementioned procedure. Then, the solids were dried and calcined to obtain the NiCo/MgO-Al₂O₃ and NiCo/ZnO-Al₂O₃ designated as NiCo/MA and NiCo/ZA, respectively.

The pure alumina was prepared as reference material and the catalytic results compared with those of NiCo catalysts supported on the modified alumina in study. Details about the synthesis are given elsewhere [21].

3.3. Characterizations

The powder X-ray diffraction (XRD) patterns were recorded in a Shimadzu XRD6000 (Shimadzu, Kyoto, Japan) diffractometer using a Cu-K α monochromatized radiation source at 40 kV and 30 mA ($\lambda = 0.154$ nm). The data were collected in the 2 θ range of 10–70° in a step-scan mode of 0.02° s⁻¹. The Joint Committee on Powder Diffraction files was used as reference to compare the obtained XRD patterns.

Fourier transform infrared spectroscopy (FTIR) spectra were collected in a Bruker equipment (Bruker, Rheinstetten, Germany) in the range of 400–4000 cm⁻¹ with a resolution of 2 cm⁻¹. Before measurements, the self-supporting KBr disks were prepared by dilution of 1 wt.% of the samples in KBr.

Raman measurements were recorded using a LabRAM HORIBA HR Evolution model, which was equipped with a CCD detector (Horiba, Gloucestershire, UK). Room-temperature Raman spectra were excited at 532 nm with $600 \text{ gr}\cdot\text{mm}^{-1}$ grating using a He-Ne laser. The laser power was set at 2 mW on the sample surface. All spectra have been recorded in the $100\text{--}1800 \text{ cm}^{-1}$ range with a spectral resolution of 4 cm^{-1} .

The morphology of samples was investigated by Scanning electron microscopy (SEM) analyses in a Quanta-FEG FEI electron microscope (FEI Quanta, Hillsboro, OR, USA). The elemental distributions of the solids were obtained in an EDX Link Analytical QX-20000 system coupled to the SEM microscope at 2 kV acceleration voltage. Previously, the samples were sputtered with Ag to perform the analyses.

The surface area, pore volume and average pore sizes were determined by N_2 physisorption isotherms at $-196 \text{ }^\circ\text{C}$, using an ASAP 2000 Micromeritics equipment instrument. Prior to analyses, samples were treated at $250 \text{ }^\circ\text{C}$ under vacuum for 2 h. The specific surface areas were using the Brunauer-Emmet-Teller (BET) equation from the adsorption branch of the isotherms, whereas pore size distributions were determined by the Barret-Joyner-Halenda (BJH) method.

Electron paramagnetic resonance (EPR) spectra were performed on a Bruker spectrometer (Bruker, Rheinstetten, Germany) with frequency modulation of 100 kHz. The EPR spectra were obtained at the X-band microwave frequencies at 9.5 GHz. The values of g were obtained by the EPR marker from module ER031, which was adjustable to mark $g = 2.0040$.

Acid properties of the catalysts were analyzed using Temperature programmed ammonia desorption (TPD- NH_3). The curves were recorded Chembet-3000 Quantachrome. Approximately 100 mg of the solids were placed on U-tube and then heated under flowing helium at $120 \text{ }^\circ\text{C}$ for 2 h. The catalyst was cooled to $100 \text{ }^\circ\text{C}$ and subsequently, a 5% of NH_3 diluted in He was placed into the tube. Thereafter, the physically adsorbed ammonia was flushed with helium for 1 h. The ammonia desorption was conducted from 50 a $350 \text{ }^\circ\text{C}$ to obtain the TPD curves.

Transmission electron microscopy (TEM) micrographs were collected on a JEOL JEM 2010F microscope with an accelerating voltage of 200 kV (Texas, TX, USA). Before the analyses, samples were treated in ethanol, sonicated and deposited on carbon-coated copper.

X-ray photoelectron spectra (XPS) were conducted on a Physical Electronics Versa Probe II Scanning XPS Microprobe (Minneapolis, MN, USA) spectrometer equipped with a monochromatic Al $\text{K}\alpha$ radiation source. Spectra were fitted by using the Gaussian-Lorentzian. The spectra were corrected to the adventitious carbon component (284.8 eV) of the C 1s region. The Multipack software version 9.6.0.15 was employed to obtain the XPS spectra.

3.4. Catalyst Testing

A typical esterification of glycerol in the presence of acetic acid reaction was carried out in a jacketed 30 mL three-necked round bottom flask reactor, which was equipped with a condenser. The composition of the reaction mixture was glycerol and acetic acid to have a glycerol to acetic acid molar ratio of 0.33. The catalyst (50 mg) was placed in the batch reactor followed by addition of the reaction mixture under vigorous stirring at 1000 rpm for a certain period of time.

Unless otherwise specified, the reaction temperature measured by a thermocouple placed into the solution was $80 \text{ }^\circ\text{C}$. The analysis system consisted in a Shimadzu gas-chromatography equipped with a capillary column and a flame ionization detector (FID). The liquid products of the reaction mixture were withdrawn periodically during the reaction course at each 60 min intervals and analyzed in the GC chromatograph. The EG esterification products were also identified by gas chromatography-mass spectroscopy (GC-MS).

The effects of the reaction time, temperature and glycerol to acetic acid were also examined. The catalyst reusability was carried out over the most active solids by recovering the

solid from the reaction mixture and adding a fresh substrate at 80 °C. Each catalyst recycle experiment was performed in 24 h intervals at least 1–4 times. Before each reuse, catalysts were separated by centrifugation, washed with ethanol and dried at room temperature. An additional loading of the solid was added to the runs to ensure 3–5% of the catalyst in the reaction media.

The catalytic performance of solids was estimated in terms of the glycerol conversion ratio (X_{gly} , Equation (1)), selectivity to the products (S , Equation (2)), the initial reaction rate is calculated for all catalysts after 0.5 h of reaction (a , Equation (3)), as follows:

$$\% X(t) = \frac{[\% \text{glyin} - \% \text{glyout}]}{\% \text{glyin}} \times 100 \quad (1)$$

where %glycerol in is the percentage by mass of inlet glycerol concentration, and %glycerol out is the percentage by mass of outlet glycerol concentration time t (h).

Selectivity was calculated according to the equation:

$$\% S = \frac{\text{Percentage of desired product}}{\text{Sum of the percentages of products formed}} \times 100 \quad (2)$$

$$\% \text{Initial rate} = \frac{\text{mmol glycerol converted}}{\text{catalysts mass} \times \text{time}} \quad (3)$$

4. Conclusions

Porous MgO-Al₂O₃, La₂O₃-Al₂O₃ or ZnO-Al₂O₃ supports with controllable acidity were modified with well dispersed Ni and Co nanoparticles. XRD, Raman and FTIR results demonstrated the prevalence of γ -Al₂O₃ with modulated porosity and acidity. EPR and XPS analyses also confirmed the existence of lattice oxygen species as well as Ni²⁺ and Co³⁺/Co²⁺ active species, enhancing the catalytic performance. This was attributed to a synergistic effect between the nanoparticles and the porous support, rather than acidity improving the activity of the solids in the EG reaction. The effects of temperature, glycerol to acetic acid molar ratios, and reusability studies surely demonstrated that the Ni and Co nanoparticles interacted strongly and well with the support and promoted the best performance of NiCo/MgO-Al₂O₃ and NiCo/La₂O₃-Al₂O₃ compared to NiCo/ZnO-Al₂O₃. In this regard, the presence of Ni and Co active sites helped by the spinel MgAl₂O₄ phase possessing high stability and a large amount of lattice oxygen species provided NiCo/MgO-Al₂O₃ to achieve superior catalytic performance in all reaction conditions. The catalyst had a good durability after being reused four times, revealing an excellent catalytic activity for the acetins production.

Supplementary Materials: The following supporting information can be downloaded at: <https://www.mdpi.com/article/10.3390/catal12121616/s1>, Figure S1: (A) SEM images, (B) EDS images and (C) EDS mapping of the unsupported solids. The numbers 1, 2 and 3 at the right side of the letters represent the LA, MA and ZA samples. Figure S2: (A) SEM images, (B) EDS images and (C) EDS mapping of the supported solids. The numbers 1, 2 and 3 at the right side of the letters represent the LA, MA and ZA samples. Figure S3: Schematic illustration of the (a) synthesis of the supports and (b) NiCo impregnation on the supports.

Author Contributions: R.d.C.F.B., G.M., J.V.d.C., R.M.B.V., R.L., L.O. and J.J.J. performed the experiments; A.C.O. and E.R.-C. analyzed the data and wrote the manuscript, funding acquisition and conceptualization; R.M.B.V. analyzed the data; G.D.S. and A.C. designed and performed the experiments and analyzed the data, as well. All authors have read and agreed to the published version of the manuscript.

Funding: This work is supported by Funcap (Grant n° PS1-0186-00346.01.00/21). Financial assistance received from Ministerio de Ciencia e Innovación, Junta de Andalucía and FEDER is also thankfully acknowledged for funding project n° PID2021-126235OB-C32, UMA18-FEDERJA-126 and P20_00375.

Acknowledgments: The Central Analítica da Universidade Federal do Ceará facility is gratefully acknowledged. R.C.F.B. would like to acknowledge support received from the CAPES for her PhD scholarship.

Conflicts of Interest: The authors declare no conflict of interest.

References

1. Koranian, P.; Huang, Q.; Dalai, A.K.; Sammynaiken, R. Chemicals Production from Glycerol through Heterogeneous Catalysis: A Review. *Catalysts* **2022**, *12*, 897. [[CrossRef](#)]
2. Neto, A.B.S.; Oliveira, A.C.; Rodríguez-Castellón, E.; Campos, A.F.; Freire, P.T.C.; Sousa, F.F.F.; Filho, J.M.; Araujo, J.C.S.; Lang, R. A comparative study on porous solid acid oxides as catalysts in the esterification of glycerol with acetic acid. *Catal. Today* **2020**, *349*, 57–67. [[CrossRef](#)]
3. Perez, F.M.; Gatti, M.N.; Nichio, N.N.; Pompeo, F. Bio-additives from glycerol acetylation with acetic acid: Chemical equilibrium model. *Results Eng.* **2022**, *15*, 100502. [[CrossRef](#)]
4. Checa, M.; Nogales-Delgado, S.; Montes, V.; Encinar, J.M. Recent Advances in Glycerol Catalytic Valorization: A Review. *Catalysts* **2020**, *10*, 1279. [[CrossRef](#)]
5. Mota, G.; do Carmo, J.V.C.; Paz, C.B.; Saraiva, G.D.; Campos, A.; Duarte, G.; Filho, E.C.S.; Oliveira, A.C.; Soares, J.M.; Rodríguez-Castellón, E.; et al. Influence of the Metal Incorporation into Hydroxyapatites on the Deactivation Behavior of the Solids in the Esterification of Glycerol. *Catalysts* **2022**, *12*, 10. [[CrossRef](#)]
6. Abida, K.; Ali, A. A review on catalytic role of heterogeneous acidic catalysts during glycerol acetylation to yield acetins. *J. Indian Chem. Soc.* **2022**, *99*, 100459. [[CrossRef](#)]
7. Carvalho, D.C.; Pinheiro, L.G.; Oliveira, A.C.; Millet, E.R.C.; de Sousa, F.F.; Saraiva, G.D.; da Silva Filho, E.C.; Fonseca, M.G. Characterization and catalytic performances of copper and cobalt-exchanged hydroxyapatite in glycerol conversion for 1-hydroxyacetone production. *Appl. Catal. A Gen.* **2014**, *471*, 39–49. [[CrossRef](#)]
8. Carvalho, D.C.; Souza, H.S.A.; Filho, J.M.; Assaf, E.M.; Thyssen, V.V.; Campos, A.; Padron Hernandez, E.; Raudel, R.; Oliveira, A.C. Nanosized Pt-containing Al₂O₃ as an efficient catalyst to avoid coking and sintering in steam reforming of glycerol. *RSC Adv.* **2014**, *4*, 61771–61780. [[CrossRef](#)]
9. Zada, B.; Kwon, M.; Kim, S.-W. Current Trends in Acetins Production: Green versus Non-Green Synthesis. *Molecules* **2022**, *27*, 2255. [[CrossRef](#)]
10. Alves, N.F.; Neto, A.B.S.; Bessa, B.D.S.; Oliveira, A.C.; Mendes Filho, J.; Campos, A.F. Binary Oxides with Defined Hierarchy of Pores in the Esterification of Glycerol. *Catalysts* **2016**, *6*, 151. [[CrossRef](#)]
11. Testa, M.L.; La Parola, V.; Liotta, L.F.; Venezia, A.M. Screening of different solid acid catalysts for glycerol acetylation. *J. Mol. Catal. A Chem.* **2013**, *367*, 69–76. [[CrossRef](#)]
12. Mou, R.; Wang, X.; Wang, Z.; Zhang, D.; Yin, Z.; Lv, Y.; Wei, Z. Synthesis of fuel bioadditive by esterification of glycerol with acetic acid over hydrophobic polymer-based solid acid. *Fuel* **2021**, *302*, 121175. [[CrossRef](#)]
13. Carmo, J.V.C.; Oliveira, A.C.; Araújo, J.C.S.; Campos, A.; Duarte, G.C.S. Synthesis of highly porous alumina-based oxides with tailored catalytic properties in the esterification of glycerol. *J. Mater. Res.* **2018**, *33*, 3625–3633. [[CrossRef](#)]
14. Zhou, L.; Al-Zaini, E.; Adesina, A.A. Catalytic characteristics and parameters optimization of the glycerol acetylation over solid acid catalysts. *Fuel* **2013**, *103*, 617–625. [[CrossRef](#)]
15. Kong, P.S.; Aroua, M.K.; Daud, W.M.A.W.; Lee, H.V.; Cognet, P.; Perez, Y. Catalytic role of solid acid catalysts in glycerol acetylation for the production of bio-additives: A review. *RSC Adv.* **2016**, *6*, 68885. [[CrossRef](#)]
16. Gao, X.; Zhu, S.; Li, Y. Graphene oxide as a facile solid acid catalyst bioadditives from glycerol esterification. *Catal. Commun.* **2015**, *62*, 48–51. [[CrossRef](#)]
17. Ferreira, F.B.; Silva, M.J.; Rodrigues, F.Á.; Faria, W.L.S. Sulfated-Alumina-Catalyzed Triacetin Synthesis: An Optimization Study of Glycerol Esterification. *Ind. Eng. Chem. Res.* **2022**, *61*, 4235–4243. [[CrossRef](#)]
18. Pankajakshan, A.; Pudi, S.M.; Biswas, P. Acetylation of Glycerol over Highly Stable and Active Sulfated Alumina Catalyst: Reaction Mechanism, Kinetic Modeling and Estimation of Kinetic Parameters. *J. Chem. Technol. Biotechnol.* **2018**, *50*, 98–111. [[CrossRef](#)]
19. Ramalingam, R.J.; Radhika, T.; Adam, F.; Dolla, T.H. Acetylation of glycerol over bimetallic Ag–Cu doped rice husk silica based biomass catalyst for bio-fuel additives application. *Int. J. Ind. Chem.* **2016**, *7*, 187–194. [[CrossRef](#)]
20. Kale, S.S.; Armbruster, U.; Eckelt, R.; Bentrup, U.; Umbarkar, S.B.; Dongare, M.K.; Martin, A. Understanding the role of Keggin type heteropolyacid catalysts for glycerol acetylation using toluene as an entrainer. *Appl. Catal. A Gen.* **2016**, *527*, 9–18. [[CrossRef](#)]
21. Araújo, J.C.S.; Oton, L.F.; Oliveira, A.C.; Lang, R.; Otubo, L.; Bueno, J.M.C. On the role of size controlled Pt particles in nanostructured Pt-containing Al₂O₃ catalysts for partial oxidation of methane. *Int. J. Hydrogen Energy* **2019**, *447*, 27329–27342. [[CrossRef](#)]
22. Nascimento, J.P.S.; Oliveira, A.C.; Araujo, J.C.S.; Sousa, F.F.; Saraiva, G.D.; Rodríguez-Aguado, E.; Rodríguez-Castellón, E. Combined promoting effect of molybdenum on the bimetallic Al₂O₃–La₂O₃ catalysts for NO_x reduction by CO. *Fuel* **2020**, *275*, 117872. [[CrossRef](#)]

23. Kirszensztejn, P.; Przekop, R.; Szymkowiak, A.; MaćkowskabJerzy, E.; Gaca, J. Preparation of MgO–Al₂O₃ binary gel system with mesoporous structure. *Microporous Mesoporous Mater.* **2006**, *89*, 150–157. [[CrossRef](#)]
24. Tantirungrotechai, J.; Chotmongkolsap, P.; Pohmakotr, M. Synthesis, characterization, and activity in transesterification of mesoporous Mg–Al mixed-metal oxides. *Microporous Mesoporous Mater.* **2010**, *128*, 41–47. [[CrossRef](#)]
25. Gonullu, M.P. Design and characterization of single bilayer ZnO/Al₂O₃ film by ultrasonically spray pyrolysis and its application in photocatalysis. *Micro Nanostruct.* **2020**, *164*, 107113. [[CrossRef](#)]
26. Abdollahifar, A.; Haghighi, M.; Babaluo, A.A.; Talkhoncheg, S.K. Sono-synthesis and characterization of bimetallic Ni–Co/Al₂O₃–MgO nanocatalyst: Effects of metal content on catalytic properties and activity for hydrogen production via CO₂ reforming of CH₄. *Ultrason. Sonochem.* **2016**, *31*, 173–183. [[CrossRef](#)]
27. Hilli, Y.; Kinnunen, N.K.; Suvanto, M.; Savimäki, A.; Kallinen, K.; Pakkanen, T.A. Sulfur adsorption and release properties of bimetallic Pd–Ni supported catalysts. *J. Mol. Catal. A Chem.* **2015**, *408*, 161–171. [[CrossRef](#)]
28. Charisiou, N.D.; Italiano, C.; Pino, L.; Sebastian, V.; Vita, A.; Goula, M.A. Hydrogen production via steam reforming of glycerol over Rh/g–Al₂O₃ catalysts modified with CeO₂, MgO or La₂O₃. *Renew. Energy* **2020**, *162*, 908–925. [[CrossRef](#)]
29. Liang, D.; Hu, Y.; Xiao, C.; Wang, G.; Xie, J.; Zhu, X. Highly efficient catalytic ozonation for ammonium in water upon γ -Al₂O₃@Fe/Mg with acidic-basic sites and oxygen vacancies. *Sci. Total Environ.* **2022**, *834*, 155278. [[CrossRef](#)]
30. Silva, A.N.; Neto, A.B.S.; Oliveir, A.C.; Junior, M.C.; Junior, J.A.L.; Freire, P.T.C.; Filho, J.M.; Oliveira, A.C.; Lang, R. Raman studies of nanocomposites catalysts: Temperature and pressure effects of CeAl, CeMn and NiAl oxides. *Spectrochim. Acta Part A* **2018**, *198*, 160–167. [[CrossRef](#)]
31. Aminzadeh, A.; Sarikhani-fard, H. Raman spectroscopic study of Ni:Al₂O₃ catalyst. *Spectrochim. Acta Part A* **1999**, *55*, 1421–1425. [[CrossRef](#)]
32. Jindal, K.; Tomar, M.; Katiyar, R.S.; Gupta, V. Raman scattering and photoluminescence investigations of N doped ZnO thin films: Local vibrational modes and induced ferromagnetism. *J. Appl. Phys.* **2016**, *120*, 135305. [[CrossRef](#)]
33. Gonçalves, A.A.S.; Costa, M.J.F.; Zhang, L.; Ciesielczyk, F.; Jaroniec, M. One-Pot Synthesis of MeAl₂O₄ (Me = Ni, Co, or Cu) Supported on γ -Al₂O₃ with Ultralarge Mesopores: Enhancing Interfacial Defects in γ -Al₂O₃ To Facilitate the Formation of Spinel Structures at Lower Temperatures. *Chem. Mater.* **2018**, *30*, 436–446.
34. Luo, M.-F.; Fang, P.; He, M.; Xie, Y.-L. In situ XRD, Raman, and TPR studies of CuO/ Al₂O₃ catalysts for CO oxidation. *J. Mol. Catal. A Chem.* **2005**, *239*, 243–248. [[CrossRef](#)]
35. Chan, S.S.; Wachs, I.E. In Situ Laser Raman Spectroscopy of Nickel Oxide Supported on γ -Al₂O₃. *J. Catal.* **1987**, *103*, 224–227. [[CrossRef](#)]
36. Escudero, M.J.; Mendoza, L.; Cassir, M.; Gonzalez, T.; Daza, L. Porous nickel MCFC cathode coated by potentiostatically deposited cobalt oxide II. Structural and morphological behavior in molten carbonate. *J. Power Sources* **2006**, *160*, 775–781. [[CrossRef](#)]
37. Nadeina, K.A.; Kazakova, M.O.; Kovalskaya, A.A.; Danilova, I.G.; Cherepanova, S.V.; Danilevich, V.V.; Gerasimova, E.Y.; Prosvirin, I.P.; Kondrashev, D.O.; Kleimenov, A.V.K.; et al. Influence of alumina precursor on silicon capacity of NiMo/ γ - Al₂O₃ guard bed catalysts for gas oil hydrotreating. *Catal. Today* **2020**, *353*, 53–62. [[CrossRef](#)]
38. Núñez, S.; Escobar, J.; Vázquez, A.; Reyes, J.A.; Hernández-Barrera, M. 4,6-Dimethyl-dibenzothiophene conversion over Al₂O₃–TiO₂-supported noble metal catalysts. *Mater. Chem. Phys.* **2011**, *126*, 237–247. [[CrossRef](#)]
39. Thommes, M.; Kaneko, K.; Neimark, A.V.; Olivier, J.P.; Rodríguez-Reinoso, F.; Rouquerol, J.; Sing, K.S.W. Physisorption of gases, with special reference to the evaluation of surface area and pore size distribution (IUPAC Technical Report). *Pure Appl. Chem.* **2015**, *87*, 1051–1069. [[CrossRef](#)]
40. Kunde, G.B.; Yadav, G.D. Green approach in the sol-gel synthesis of defect free unsupported mesoporous alumina films. *Microporous Mesoporous Mater.* **2016**, *224*, 43–50. [[CrossRef](#)]
41. Wang, L.; Liu, H.; Fan, Y.; Yuan, P.; Huang, D.; Oyama, T.; Wang, S.T.; Bao, X. Cooperative bimetallic catalyst for thio-etherification reaction prepared by crystal-facet engineering of γ -Al₂O₃ support. *Catal. Today* **2021**, *377*, 196–204. [[CrossRef](#)]
42. Nguyen, T.T.; Tsai, H.D.-H. Low-temperature methanol synthesis via (CO₂ + CO) combined hydrogenation using Cu–ZnO/Al₂O₃ hybrid nanoparticle cluster. *Appl. Catal. A Gen.* **2022**, *645*, 118844. [[CrossRef](#)]
43. Jiang, T.; Kong, D.; Xu, K.; Cao, F. Hydrogenolysis of glycerol aqueous solution to glycols over Ni–Co bimetallic catalyst: Effect of ceria promoting. *Appl. Petrochem. Res.* **2016**, *6*, 135–144. [[CrossRef](#)]
44. Tsiotsias, A.I.; Charisiou, N.D.; Sebastian, V.; Gaber, S.; Hinder, S.J.; Baker, M.A.; Polychronopoulou, K.; Goula, M.A. A comparative study of Ni catalysts supported on Al₂O₃, MgO–CaO– Al₂O₃ and La₂O₃– Al₂O₃ for the dry reforming of ethane. *Int. J. Hydrogen Energy* **2022**, *14*, 5337–5353. [[CrossRef](#)]
45. Ju, F.; Liu, C.; Li, K.; Meng, C.; Gao, S.; Lin, H. Reactive Adsorption Desulfurization of Fluidized Catalytically Cracked (FCC) Gasoline over a Ca-Doped Ni–ZnO/ Al₂O₃ –SiO₂ Adsorbent. *Energy Fuels* **2016**, *30*, 6688–6697. [[CrossRef](#)]
46. Yamamoto, T.; Hatsui, T.; Matsuyama, T.; Tanaka, T.; Funabiki, T. Structures and Acid–Base Properties of La/Al₂O₃ Role of La Addition to Enhance Thermal Stability of γ -Al₂O₃. *Chem. Mater.* **2003**, *15*, 4830–4840. [[CrossRef](#)]
47. Nikolova, D.; Edreva-Kardjieva, R.; Gouliev, G.; Grozeva, T.; Tzvetkov, P. The state of (K)(Ni)Mo/g–Al₂O₃ catalysts after water–gas shift reaction in the presence of sulfur in the feed: XPS and EPR study. *Appl. Catal. A Gen.* **2006**, *297*, 135–144. [[CrossRef](#)]
48. Zhu, J.; Cannizzaro, F.; Liu, L.; Zhang, H.; Kosinov, N.; Filot, I.A.W.; Rabeah, J.; Brückner, A.; Hensen, E.J.M. Ni–In Synergy in CO₂ Hydrogenation to Methanol. *ACS Catal.* **2021**, *11*, 11371–11384. [[CrossRef](#)]

49. Zhang, Z.-H.; Wu, S.-Y.; Xu, P.; Li, L.-L. Theoretical studies of the EPR parameters for Ni²⁺ and Co²⁺ in MgO. *Braz. J. Phys.* **2010**, *40*, 361. [[CrossRef](#)]
50. Natte, K.; Jagadeesh, R.V.; Sharif, M.; Neumann, H.; Beller, M. Synthesis of Nitriles from Amines using Nanoscale Co₃O₄ -based Catalysts via Sustainable Aerobic Oxidation. *Org. Biomol. Chem.* **2016**, *14*, 3356–3359. [[CrossRef](#)]
51. Silva-Calpa, L.R.; Zonetti, C.; Rodrigues, C.P.; Alves, O.C.; Appel, L.G.; de Avillez, R.R. The Zn_xZr_{1-x}O_{2-y} solid solution on m-ZrO₂: Creating O vacancies and improving the m-ZrO₂ redox properties. *J. Mol. Catal. A Chem.* **2016**, *425*, 166–173. [[CrossRef](#)]
52. Carmo, J.V.; Bezerra, R.C.F.; Tehuacanero-Cuapa, S.; Rodríguez-Aguado, E.; Lang, R.; Campos, A.F.; Duarte, G.; Saraiva, G.D.; Otubo, L.; Oliveira, A.C.; et al. Synthesis of tailored alumina supported Cu-based solids obtained from nanocomposites: Catalytic application for valuable aldehyde and ketones production. *Mater. Chem.* **2022**, *292*, 126800. [[CrossRef](#)]
53. Manríquez-Ramírez, M.E.; Elizalde, I.; Ramírez-López, R.; Trejo-Valdez, M.; Estrada-Flores, M. Acetylation of glycerol using MgO–CaO catalysts with different CaO loadings. *React. Kinet. Mech. Catal.* **2020**, *130*, 417–431. [[CrossRef](#)]
54. Rane, S.A.; Pudi, S.M.; Biswas, P. Esterification of Glycerol with Acetic Acid over Highly Active and Stable Alumina-based Catalysts: A Reaction Kinetics Study. *Chem. Biochem. Eng. Q.* **2016**, *30*, 33–45. [[CrossRef](#)]
55. Tentor, F.R.; Dias, D.B.; Gomes, M.R.; Vicente, J.G.; Cardozo-Filho, P.L.; Berezuk, M.E. Glycerol Acetylation with Propionic Acid Using Iron and Cobalt Oxides in Al-MCM-41 Catalysts. *Bull. Chem. React. Eng. Catal.* **2020**, *15*, 803. [[CrossRef](#)]
56. Malaik, A.; Ptaszyński, K.; Kozłowski, M. Conversion of renewable feedstock to bio-carbons dedicated for the production of green fuel additives from glycerol. *Fuel* **2021**, *288*, 119609. [[CrossRef](#)]